Dynamic profiling and functional interpretation of histone lysine crotonylation and lactylation during neural development

Shang-Kun Dai[1,2,3], Pei-Pei Liu[1,3], Zhao-Qian Teng[1,2,3], and Chang-Mei Liu[1,2,3,4,*]

[1]State Key Laboratory of Stem Cell and Reproductive Biology, Institute of Zoology, Chinese Academy of Sciences, Beijing 100101, China.

[2]Savaid Medical School, University of Chinese Academy of Sciences, Beijing 100049, China.

[3]Institute for Stem Cell and Regeneration, Chinese Academy of Sciences, Beijing 100101, China.

*Corresponding author. Tel: +86-10-82619690; Email: liuchm@ioz.ac.cn

Running title: Characterization of histone lysine acylations during neural development

Keywords: Histone lysine crotonylation, histone lysine lactylation, transcriptional regulation, neural development, histone deacetylases

Abstract

Metabolites such as crotonyl-CoA and lactyl-CoA influence gene expression through covalently modifying histones, known as histone lysine crotonylation (Kcr) and histone lysine lactylation (Kla). However, we do not know their dynamic changes, biological functions and associations with histone lysine acetylation (Kac) in vivo and during development. Here, we profile H3K9ac, H3K9cr and H3K18la in the developing telencephalon, and find that genome-wide alterations of these histone marks collaboratively regulate transcriptome remodelling to favour neural differentiation. We also demonstrate that global histone Kcr and Kla levels are not affected by transcription inhibition. Importantly, we identify HDAC1-3 as novel “erasers” of H3K18la and furtherly show that a selective inhibitor of HDAC1-3, MS-275 promotes transcriptional programs associated with neural cell fate decisions via H3K18la. Taken together, our results uncover the interplays between histone lysine acylations to regulate gene expression and the differentiation-promoting functions of histone Kcr and Kla during development.

Introduction

The N-terminal tails of histones are subjected to various post-translational modifications (PTMs), which shape local chromatin landscape to regulate transcription, replication, DNA repair and higher-order chromatin structure [1, 2]. Some metabolites have recently been reported as donors for histone PTMs to influence gene expression, including propionyl-CoA, butyl-CoA, crotonyl-CoA, lactyl-CoA, 2-hydroxyisobutyl-CoA, β-hydroxybutyryl-CoA, malonyl-CoA, succinyl-CoA and glutaryl-CoA [1, 3]. Of these, crotonyl-CoA and lactyl-CoA, which act as substrates for histone lysine crotonylation (Kcr) and lysine lactylation (Kla) reactions catalysed by p300/CBP respectively [4, 5], have attracted increasing attention due to their emerging roles in linking cellular metabolism and epigenetic regulation to orchestrate gene expression, development and diseases progression [5-8].

Kcr and Kla have been identified in both histones 2A, 2B, 3 and 4, and they share the most common modification sites with Kac [5, 9]. Over the last five years, regulatory mechanisms of histone Kcr have been thoroughly explored, including its "writers" (enzymes in charge of catalysing Kcr) [4, 10, 11], "erasers" (enzymes responsible for removing Kcr) [12-14], "readers" (enzymes capable of recognising Kcr) [15-18], and metabolic regulators (enzymes involving in crotonyl-CoA metabolism) [4, 19-23], which extend our knowledge about biological functions of histone Kcr. Recent studies have demonstrated that p300 and glycolysis are major pathways to regulate histone Kla levels, and that H3K18la plays key roles in M1 macrophage polarization, cell reprograming and tumorigenesis [5, 7, 8]. Both histone Kcr and Kla can directly stimulate gene transcription using reconstituted chromatin-templated transcription in a cell free system [4, 5]. For histone Kcr, recognition of H3K9cr, H3K18cr and H3K27cr by YEATS domain of AF9 may regulate transcription though recruiting Super Elongation Complex (SEC) and Dot1L complex (DOT1LC) [15, 24, 25]. However, it is unclear whether the link between histone Kcr and Kla and transcription is causal or consequential in cells or in vivo under physiological conditions.

Positive association between levels of H3K9cr, H3K18cr, H3K27cr, histone Kcr and gene expression has been reported in various organisms [4, 9, 12, 14, 26-28]. Recently, histone Kla has been suggested as a metabolic stress-related histone modification, which is associated with the polarization of bacterially challenged M1 macrophages and the tumorigenesis of ocular melanoma [5, 7]. Given that histone Kac plays important roles in proliferation and differentiation of neural stem/progenitor cells (NSPCs) [29-31], however, it remains unknown whether and how histone Kcr and Kla involve in transcription regulation during neural development.

In the current study, we investigate the dynamic changes and associations with chromatin accessibility and gene expression of histone Kcr and Kla, as well as interplays among histone lysine acylations during neural development. We observe the global existence and dynamic changes of H3K9cr, H3K18cr, H3K14la and H3K18la in the developing telencephalon. Further multi-omics profiling uncovers that H3K9cr and H3K18la mark transcriptionally active chromatin state, but differ

in signal pathways they involved both in vivo and in cells. Although there are distinct patterns of genome-wide alterations of H3K9ac, H3K9cr and H3K18la, in-depth comparisons of chromatin immunoprecipitation-sequencing (ChIP-seq) and RNA-seq data at different neural developmental stages reveal that these histone marks collaboratively regulate transcriptome remodelling to favour neural differentiation. In addition, inhibition of transcription dose not influence global histone Kcr and Kla levels. Finally, we discover that HDAC1-3 repression increases H3K18la levels which are associated with the acquisition of neural fate in the differentiating P19 embryonal carcinoma (EC) cells.

Results

Global changes of histone Kcr and Kla levels during neural development

We firstly determined the presence of H3K9cr, H3K18cr, H3K14la and H3K18la in the embryonic telencephalon. The results demonstrated that these histone marks exhibited extensive existence in the germinal zones with strong staining signals of all four antibodies (Fig 1A; S1A Fig). Subsequently, we detected the levels of these histone marks across different developmental stages, and found that H3K9cr and H3K18cr levels increased but H3K18la and H3-Kla levels reduced at late-stage neurogenesis compared with early-stage neurogenesis, however, there were no changes of H3K14la and H3-Kcr levels in the developing telencephalon (Fig 1B; S1B-S1D Fig).

We then checked the global changes of these histone marks at different stages of neural differentiation in cells (S1E Fig). The results showed that these histone marks could be observed in both Nestin^{+} NSPCs and TUJ1^{+} neurons derived from P19 EC cells (Fig 1C). Interestingly, the levels of H3K18cr and H3K18la, but not H3K9cr and H3K14la declined sharply during neural differentiation of P19 EC cells (Fig 1D; S1F Fig), which indicated distinct dynamic changes of site-specific histone lysine acylations during neural cell fate decision. Altogether, these results suggest that histone Kcr and Kla are widely distributed and undergo global changes during neural development.

Multi-omic profiling and functional interpretation of H3K9cr and H3K18la

In order to explore the chromatin function of histone Kcr and Kla in neural development, we performed specific anti-H3K9ac, H3K9cr and H3K18la (lactylation is not found at H3K9 site in mouse cells) ChIP-seq assays of the telencephalon at E13.5 (S2 Fig) [5], and generated highly reproducible sequencing data (S3A Fig). The results suggested that the majority of H3K9ac and H3K9cr peaks were located in the promoter regions, while H3K18la peaks were mainly distributed in the intron and intergenic regions (Fig 2A). Immediately, k-means clustering of the annotated genes revealed that gene loci with higher levels of H3K9ac were usually accompanied with higher levels of H3K9cr, H3K18la, chromatin accessibility as well as gene expression (Fig 2B). Furthermore, genes with all three marks displayed the higher chromatin accessibility in the promoter regions and higher gene expression levels than that of the mono-marked genes (Fig 2C). Interestingly,

H3K9ac-marked genes were also modified with H3K9cr and H3K18la, while more than 4000 genes were marked by H3K18la only (S2B Fig). These results suggested that different types of histone lysine acylations might co-contribute to transcriptionally active chromatin state.

In our analysis, we found that there were many genes marked by these modifications with different levels of histone lysine acylation (S3B and S3C Fig). Therefore, we divided peaks into three clusters based on their modification levels to interpret biological functions of these histone marks (S3C Fig). Interestingly, genes with the strongest H3K9cr intensity (cluster 1) were annotated in RNA and protein metabolism and neurodegenerative disorders-related KEGG pathways, however, genes with the highest H3K18la levels were mainly involved in cell proliferation-related pathways (Fig 2D). Consistently, our ChIP-seq assays of these histone marks using P19 EC cells-derived NSPCs confirmed their interplays and important functions at the cell level (S4 Fig). Thus, these results indicate that H3K9ac, H3K9cr and H3K18la exhibit cooperative regulation of chromatin state and gene expression, but they are involved in different signalling pathways in vivo and in cells.

Genome-wide alterations in H3K9cr and H3K18la regulate transcriptome remodelling to favour neural differentiation in vivo

Histone marks undergo dynamic changes and play important roles during embryonic neurogenesis in which NSPCs exit cell cycle and differentiate into neurons [31]. However, it is still not clear how histone Kcr and Kla participate in this process. Therefore, we compared genome-wide changes of H3K9ac, H3K9cr and H3K18la at early (E13.5) and late (E16.5) stages of embryonic neurogenesis (S5 Fig). We first explored the association between alterations of these histone marks in the promoter regions and gene expression changes (S6A and S6B Fig), and found that genes with different binding of all three marks displayed the higher gene expression changes than genes with alterations of mono-mark (Fig 3A and 3B). Importantly, there were significant correlations between H3K9ac, H3K9cr and H3K18la enrichment and altered gene expression (S6C-S6E Fig). After checking genes with different patterns of changes of these histone marks, we found that H3K18la enrichment declined more significantly at genes encoding histones which play important roles during cell proliferation than that of H3K9ac and H3K9cr (S6F and S6G Fig) [32].

Next, we compared the peaks with different binding of H3K9ac, H3K9cr and H3K18la during neural development. Unexpectedly, changes in number of peaks and annotated genes with different binding of modifications showed distinct patterns across these histone marks (S7 Fig). For instance, H3K9ac was the mark with the most peaks and annotated genes with increased enrichment, and tailed the fewest with reduced binding comparing with H3K9cr and H3K18la. In contrast, there were more decreased H3K18la binding than increased as either the number of peaks or annotated genes versus H3K9ac and H3K9cr (S7A-S7E Fig). However, involved biological processes of genes with increased or decreased binding of all three marks were highly consistent with development program (S5 Fig; S7F and S7G Fig). To correlate the alterations of these histone marks with gene expression changes,

we performed binding and expression target analysis (BETA) [33], and revealed that H3K18la and H3K9cr peaks with increased enrichment had significant effects as a gene activator, while peaks of reduced H3K18la and H3K9cr binding could act as the predictor of down-regulated gene expression (Fig 3C-3F; S8A-S8D Fig). Further enrichment analysis showed that genes with increased H3K18la or H3K9cr enrichment and up-regulated gene expression were mainly involved in neural differentiation (Fig 3G; S8E Fig), comparatively, while genes with reduced binding of H3K18la or H3K9cr and down-regulated gene expression were tightly associated with cell proliferation (Fig 3H; S8F Fig). Collectively, although there is a huge difference in the number of peaks and annotated genes with different binding across H3K9ac, H3K9cr and H3K18la modifications, these histone marks undergo genome-wide alterations and collaborate to regulate gene expression associated with neural differentiation in vivo.

Transcription repression has no effect on global histone Kcr and Kla levels

A recent study shows that inhibition of transcription results in the loss of histone Kac in bulk histones, and majority of histone acetylation is dependent on transcription [34]. However, the associations between non-acetylation histone lysine acylations and transcription under physiological conditions are unclear. To investigate if the histone Kcr and Kla were influenced by transcription, we treated P19 EC cells-derived NSPCs (day 2) with the well-studied transcription inhibitors Triptolide (inhibiting transcription inhibition) and Flavopiridol (inhibiting transcription elongation) at higher concentrations [35, 36]. Transcription was significantly inhibited as indicated by the loss of RNA polymerase II (RNAP2) serine 5 CTD phosphorylation (S5p) and RNAP2 serine 2 CTD phosphorylation (S2p) (Fig 4A and 4B). Surprisingly, we didn't detect any significant changes of H3K9cr, H3K18cr, H3K14la and H3K18la levels (Fig 4C-4E), which indicate that majority of histone Kcr and Kla are not consequence of transcription.

HDAC1-3 inhibition stimulates the elevation of H3K18la both in cells and in vivo

Given the fact that some histone deacetylases (HDACs) have been demonstrated to "erase" various histone lysine acylations except Kac [13, 37], we next asked whether HDACs could regulate histone Kla. To this end, we applied two pan-HDACs inhibitors (SAHA and VPA), and found that SAHA treatment increased H3K18la levels while VPA stimulated both H3K14la and H3K18la in P19 EC cells (Fig 5A and 5B). Moreover, we found that a selective inhibitor of HDAC1-3, MS-275, robustly promoted the elevation of H3K14la and H3K18la comparing with EX 527 (a selective SIRT1 inhibitor) (Fig 5C). Meanwhile, we observed increased H3K9cr and H3K18cr levels after SAHA, VPA or MS-275 treatment, which were consistent with previous studies (Fig 5A-5C) [12].

To confirm our above findings in vivo, we injected pregnant mice with MS-275 and detected a significant increase in H3K14la and H3K18la levels in the embryonic telencephalon, as well as an enhancement of H3K9cr and H3K18cr levels which have not been reported previously in vivo (Fig 5D-5F). We next investigated whether the dynamic changes of histone Kla existed under interference

of expression of HDACs, the results showed that simultaneous knockdown of *Hdac1-3* increased levels of H3K18la but not global histone Kla in P19 EC cells (Fig 5G and 5H), which might be caused by different regulatory mechanisms at other histone Kla sites. Overall, these results suggest that HDAC1-3 are novel site-specific histone lysine delactylases both in cells and in vivo.

H3K18la is implicated in the upregulation of neural differentiation-related genes by MS-275

H3K18la has been demonstrated to regulate M1 macrophage polarization, cell reprograming and tumorigenesis recently [5, 7, 8], however, we still don't know how H3K18la is regulated and co-operates with other histone lysine acylations during neural cell fate determination. To this end, we treated differentiating P19 EC cells with MS-275, and performed ChIP-seq assays of H3K9ac, H3K9cr and H3K18la subsequently. HDAC1-3 inhibition by MS-275 induced genome-wide changes of H3K18la binding (Fig 6A; S9A Fig). Interestingly, increased H3K9ac and H3K9cr enrichment were also observed at peaks with the increase of H3K18la, which indicated HDAC1-3 "erase" multiple histone lysine acylations simultaneously in their binding regions (Fig 6B; S9B and S9C Fig). Furthermore, genes with increased binding of all three marks in the promoter regions displayed the higher gene expression changes than those with alterations of mono-mark after MS-275 treatment (Fig 6C).

After comprehensive comparison with H3K18la ChIP-seq data of NSPCs at day 4, we identified 1739 peaks with increased H3K18la binding in both NSPCs under MS-275 treatment (day 2) and NSPCs at day 4 comparing with that of control NSPCs at day 2 (S9D Fig). Genes annotated in these peaks were directly involved in neural differentiation (S9E Fig). Having taken gene expression changes into account, H3K18la upregulated 750 genes (S9F and S9G Fig), which could be divided into three clusters based on their patterns of expression changes across different timepoints of differentiation (Fig 6D; S9H Fig). Genes in cluster 1 were highly expressed in P19 EC cells but down-regulated during neural differentiation, and they were involved in regulation of embryonic development. Conversely, genes in cluster 2 were gradually upregulated during differentiation and participated in neural differentiation. Interestingly, genes in cluster 3 were blocked during whole neural differentiation process which might be associated with the development of other germ layers. Overall, MS-275 promotes transcriptional programs associated with neural differentiation in P19 EC cells via regulating H3K18la.

Discussion

In this study, we have profiled dynamic changes of H3K9ac, H3K9cr and H3K18la at global and genome-wide levels in the developing telencephalon and NSPCs, and demonstrate that HDAC1-3 act as novel "erasers" of H3K18la and furtherly link H3K18la with neural differentiation. First, these marks display extensive existence in the developing embryonic telencephalon and evident changes of global levels during neural development. Next, both H3K9ac, H3K9cr and H3K18la are histone

PTMs marking active chromatin regions and cooperatively regulate gene expression. Comparison of alterations of these marks during neural development reveal that genome-wide increased and decreased H3K9cr and H3K18la binding mainly involve in neural differentiation and cell proliferation processes respectively, highlighting the remodelling of these marks to orchestrate changes of gene expression and cell fate (Fig 7A). Moreover, we show that global levels of histone Kcr an Kla are not influenced by a short transcription inhibition. Importantly, we demonstrate that HDAC1-3 can "erase" H3K18la in cells and in vivo, and genes with increase in H3K18la levels after MS-275 treatment are tightly associated with neural differentiation in P19 EC cells (Fig 7B).

The extensive existence and so many marked-genes of histone Kcr and Kla in the developing telencephalon indicated that histone lysine acylations may act as universal epigenetic mechanisms to regulate gene expression during neural development. The difference in patterns of changes of H3K9ac, H3K9cr and H3K18la binding is understandable, because the levels of donors for various histone lysine acylations may alter during neural development. For instance, there is a transition from glycolytic to mitochondrial oxidative phosphorylation during neurogenesis, therefore it is possible that reduction in production of lactate and lactyl-CoA may influence dynamic changes of H3K18la and H3-Kla levels during neural development [38]. Knockdown of CBP inhibits neurogenesis in embryonic neocortex, and intermediate progenitors are prone to neural differentiation with HDAC1 and 2 deletion in forebrain [29, 30], which indicate an opposite effect of these enzymes during neural differentiation. Both CBP and H3K9/14ac are already bind the promoter of *Tuj1* (a marker of neuron) at E13, binding peaks at E16, and then decrease postnatally in the developing cortex, correlating with neurogenesis [29]. In adult brain, CBP/p300 maintain the excitatory neuron identity though the regulation of histone Kac at cell type-specific promoter and enhancer regions [39]. These results suggest important roles of CBP/p300 during establishment and maintenance of neuron identity. At early stage of neurogenesis, neural differentiation-related genes are kept in primed state, and both histone acetyltransferases (HATs) and HDACs are targeted to these development-related primed genes simultaneously [40, 41]. Based on our findings that increased H3K9ac, H3K9cr and H3K18la binding at neural differentiation-related genes accompanied by undergoing neurogenesis, as well as the capacity of CBP/p300 to catalyse histone Kac, Kcr and Kla [4, 10], we propose the existence of a switch of "actyl-spray" targeting regulatory elements of genes related to neural differentiation, which is triggered by the balance between CBP/p300 and HDACs (Fig 7A).

Almost all studies of considering the causal relationship between histone Kcr and Kla and transcription or gene expression, make their conclusions based mainly on the consistency between dynamic changes of histone marks and gene expression. However, there is no evidence to support direct regulation of transcription by histone Kcr and Kla at the cell level. In addition, whether the link between histone Kcr and Kla and transcription under physiological condition is a causal or consequential event has not been addressed previously. Although the present study can't rule out the possibility of changes of these histone marks in the local sites of the genome, our data clearly show

that transcription inhibition has no effect on global histone Kcr and Kla levels, indicating that the majority of histone Kcr and Kla are not dependent on transcription. In support of our conclusion, recent studies report that there is no global effect on histone Kac within a short time frame of transcription inhibition [42].

Recently, some HDACs have been proved to “erase” histone Kcr (HDAC1, 2, 3, 8 and SIRT1) [13], histone lysine benzoylation (Kbz, SIRT2) [37] and histone lysine β-hydroxybutyrylation (Kbhb, HDAC1 and 2) [43] in cells. Surprisingly, we find that inhibition of HDAC1-3 significantly stimulates H3K14la and H3K18la levels both in cells and in vivo, which suggest that HDAC1-3 are novel “erasers” of histone Kla. A recent study by Olsen and collaborators also report histone delactylation activity of HDAC1-3 in vitro [44]. But under physiological conditions, they find that there are no changes in H3K18la levels upon knockdown of *HADC1-3* in HeLa cells. In contrast, we observe remarkably increased H3K18la levels after simultaneous knockdown of *Hdac1-3* in NSPCs. We speculate that this discrepancy may be due to the knockdown efficiency of HDAC1-3 and the cell types. Indeed, our in vivo and ChIP-seq data do support the conclusion that HDAC1-3 can “erase” H3K18la in NSPCs. Functionally, genes with gain of H3K18la after MS-275 treatment are directly involved in neural differentiation, which indicate that HDAC1-3 inhibition leads to advanced activation of differentiation-related genes through H3K18la (Fig 7B). However, there are comparable increase of H3K18la levels across three clusters of genes with up-regulated gene expression by MS-275 (S9H Fig), but difference in the degree of the upregulation of gene expression (Fig 6D), which suggest distinct response-mechanisms to gain of H3K18la in these genes.

Overall, our study provides the first and novel insights into the dynamic changes, epigenetic interactions, transcriptional regulations and biological functions of histone lysine acylations in vivo and during neural development. Future studies should focus on how HATs and HDACs orchestrate to control different histone lysine acylations, and the underlying metabolic mechanisms behind dynamic changes of these histone marks and gene expression during development and diseases.

Materials and methods

Mice

All mice used in the current study had a ICR (CD-1) background, pregnant mice were purchased from SiPeiFu Biotechnology Co., Ltd (Beijing, China). All mouse experiments were approved by the Animal Committee of the Institute of Zoology, Chinese Academy of Sciences, Beijing, China.

Cell culture

P19 embryonal carcinoma (EC) cells were maintained in the proliferation medium (minimum essential medium-alpha (MEMα; Thermo Fisher Scientific) containing 10% fetal bovine serum (FBS; Thermo Fisher Scientific)) in an incubator at 37°C and 5% CO_2. For induced neural differentiation, 1×10^6 cells were cultured on a 9.6 cm bacterial-grade Petri dish (Greiner) in the induction medium (proliferation medium containing 1 μM all-trans retinoic acid (Sigma-Aldrich)) for 4 d, with media exchanged every 2 d. To induce neuronal differentiation, the aggregated neurospheres were digested in to single cells by Accutase (STEMCELL Technologies) and plated at a density of 1.2×10^7 cells per 10 cm culture dish (Corning) pre-coated with 0.1 mg/ml poly-D-lysine (PDL; Sigma-Aldrich) in the differentiation medium (DMEM/F12 containing with 2% B27 (Thermo Fisher Scientific)) for 4 d, with media exchanged every 2 d.

Inhibitor treatment

Inhibitors were all purchased from Selleck Chemicals. P19 EC cells treatments were performed in the proliferation medium at the following concentration for 12 h or 24 h: 0.5 μM SAHA (S1047, CAS 149647-78-9), 1 mM VPA (S3944, CAS:99-66-1), 1 μM MS-275 (S1053, CAS 209783-80-2) and 1 μM EX 527 (S1541, CAS 49843-98-3). For in vivo experiment, 20 mg/kg MS-275 was injected every 24 h for two consecutive days on pregnant mice at day 13.5 of pregnancy (E13.5-E15.5). P19 EC cells-derived NSPCs (day 1) were treated with 1 μM MS-275 for 1 d and then collected for ChIP-seq and RNA-seq assays. P19 EC cells-derived NSPCs (day 2) treatments were performed in the induced medium at the follow concentration for 1 h: 5 μM Triptolide (S3604, CAS 38748-32-2) and 5 μM Flavopiridol HCl (S2679, CAS 131740-09-5).

Cell transfection

P19 EC cells were transfected with double-strand siRNA using Lipofectamine™ RNAiMAX (Thermo Fisher Scientific) with the final concentration at 50 nM for 3 d and then collected for western blot assay. The Negative control siRNA (siR NC #1, siN0000001-1-5) and siRNA targeting Hdac1 (si-m-Hdac1_004, siB140729172936), Hdac2 (si-m-Hdac2_004, siB140729171225) and Hdac3 (si-m-Hdac3_001, siG141217112523) were purchased from Ribobio Co., Ltd (Guangzhou, China).

Immunocytochemistry and immunostaining

For immunocytochemistry analyses, cells on coverslips were fixed in 4% paraformaldehyde for 15 min at room temperature, washed three times in PBS (10-min wash each time). Next, cells were blocked in a blocking solution (2% bovine serum albumin and 0.3% Triton X-100) at room temperature for 1 h. The coverslips were then incubated with primary antibodies diluted in blocking solution at 4°C overnight, and labelled using appropriate secondary antibodies at room temperature for 2 h. For immunostaining, embryonic mouse brains were cut into 12-μm-thick cryosections using Leica CM 1950. The staining procedures for brain slices were similar with those used for immunocytochemistry described above. All images were acquired by confocal microscopy (ZEISS, LSM880) and analysed with ZEN 2012. The detailed information of the primary and secondary antibodies used were summarized in the S1 Table.

Western blot and dot blot assay

Total proteins were extracted using the RIPA lysis buffer (Beyotime Biotechnology, Shanghai, China) containing 1×complete proteinase inhibitor (Bimake), and protein concentration was defined using BCA protein assay kit (Beyotime). Histones were isolated by a modified acid extraction protocol [45]. In briefly, cells and tissues were incubated with extraction buffer (PBS with 0.5% Triton X-100, 1 mM PMSF and 5 mM sodium butyrate) with gentle rotation at 4 °C for 10 min, and nuclei were isolated by centrifugation (1500 g for 10 min at 4°C). 0.4 M HCL was used to resuspend nuclei, followed by incubation on ice for 30 min, soluble histones were isolated by centrifugation (20,000 g for 10 min at 4°C) and quantified using a Bradford protein assay kit (Beyotime).

Proteins were separated using 6-15% SDS-PAGE and transferred onto PVDF membranes (Millipore). Then, the membranes were blocked in 5% skimmed milk (BD Biosciences) in TBS-T (Tris-buffered saline with 0.1% Tween 20) and incubated with primary antibodies at 4°C overnight. The membranes were then washed in TBS-T for 10 min, three times, and incubated with secondary antibodies at room temperature for 1-2 h. The immunoreactive products were detected by using SuperSignal^{TM} West Pico PLUS Chemiluminescent Substrate (Thermo Fisher Scientific) and Tanon-5200 Chemiluminescent Imaging System (Tanon, Shanghai, China). ImageJ was then used to perform quantitative analysis of western blot results as the ratio of target histone marks or proteins *gray value* to reference proteins *gray value* (H3, β-actin or β-Tubulin). The detailed information of the primary and secondary antibodies used were summarized in the S1 Table.

For dot blot assay, peptide samples were spotted onto PVDF membranes, the membranes were first blocked at room temperature for 1 h and then washed in TBS-T. Primary and secondary antibodies were incubated at room temperature for 2 h or overnight and 45 min respectively, followed by TBS-T wash for three times and signal detection.

ATAC-seq and RNA-seq

We used the TruePrep® DNA Library Prep Kit V2 for Illumina to construct ATAC-seq libraries in two biological replicates (#TD501, Vazyme, Nanjing, China). In brief, a total of 5×10^4 cells (P19 EC cells-derived NSPCs and digested telencephalon cells at E13.5) were lysed in 50 μL lysis buffer (10 mM Tris-HCl pH 7.4, 10 mM NaCl, 3 mM $MgCl_2$ and 0.5% (v/v) NP-40) on ice for 10 min. The suspension was then centrifuged at 500 g for 5 min at 4°C, following by addition of 50 μL trans-position reaction mix containing 5×TTBL and TTE Mix V50 to incubate at 37°C for 30 min. After tagmentation, fragmented DNA was purified with 100 μL (2×) VAHTS® DNA clean beads (Vazyme) and amplified for 12 cycles using the following PCR conditions: 72 °C for 3 min; 98 °C for 30 s; and thermocycling at 98 °C for 15 s, 60 °C for 30 s and 72 °C for 30 s; following by 72 °C for 5 min. After PCR amplification, libraries were purified and selected by DNA clean beads. Libraries were then sequenced on an Illumina paired-end platform with 150 bp per read length by Annoroad Gene Technology Co., Ltd (Beijing, China).

RNA-seq was performed in two biological replicates. Briefly, RNA was extracted using Trizol™ reagent according to the instructions (Thermo Fisher Scientific) and mRNA was purified from total RNA using poly-T oligo-attached magnetic beads. Libraries were then constructed with the NEBNext® Ultra™ RNA Library Prep Kit for Illumina® (NEB) following the manufacturer's instructions and sequenced on an Illumina paired-end platform with 150 bp per read length by Annoroad Gene Technology Co., Ltd.

Native ChIP-seq

Native ChIP was carried out in two biological replicates following the published protocol with minor alterations [12]. In brief, cell pellets (P19 EC cells-derived NSPCs and digested telencephalon cells at E13.5 and E16.5) were resuspended in 500 μL swollen buffer (0.3 M sucrose, 60 mM KCl, 15 mM NaCl, 5 mM $MgCl_2$, 0.1 mM EDTA, 15 mM Tris-HCl pH 7.5, 5 mM sodium butyrate, and 1×complete proteinase inhibitor). Nuclei were isolated using an equal volume extraction buffer (0.3 M sucrose, 60 mM KCl, 15 mM NaCl, 5 mM $MgCl_2$, 0.1 mM EDTA, 15 mM Tris-HCl, pH 7.5, 0.4 % NP-40, 5 mM sodium butyrate and 1×complete proteinase inhibitor) with gentle rotation (30 rpm) at 4 °C for 10 min. The cell suspension was transferred into new tubes containing 500 μL sucrose cushion buffer (0.6 M sucrose, 60 mM KCl, 15 mM NaCl, 5 mM $MgCl_2$, 0.1 mM EDTA, 15 mM Tris-HCl pH 7.5, 5 mM sodium butyrate and 1×complete proteinase inhibitor) and centrifuge at 1500 g for 10 min at 4^oC. Nuclei were softly resuspended by MNase digestion buffer (0.32 M sucrose, 4 mM $MgCl_2$, 1 mM $CaCl_2$, 50 mM Tris-HCl pH 7.5, 5 mM sodium butyrate and 1×complete proteinase inhibitor). The amount of chromatin present in the sample was assessed by spectrophotometry in the presence of 0.1% SDS, and chromatin was then digested using Micrococcal nuclease (Takara) (1U per 10 μg chromatin) at 600 rpm in a thermomixer for 5 min at 37^oC. The reaction was stopped by adding EDTA to a final concentration of 5 mM and incubated on ice for 5 min, then cleared at 12,000 g for 10 min at 4^oC. The supernatant (S1 fraction) was stored at 4^oC and the pellet was resuspended in

dialysis buffer (0.2 mM EDTA, 1 mM Tris-HCl pH 7.5, 5 mM sodium butyrate), and then dialyse against 1.5 L dialysis buffer by Slide-A-Lyzer™ Dialysis Cassette, 10K MWCO, 3 mL (Thermo Fisher Scientific) overnight at 4°C. The dialysed pellet (S2 fraction) was cleared at 20,000 g for 10 min at 4°C and combined with S1 fraction for immunoprecipitation.

We measured the dsDNA amount of combined S1 and S2 fraction using Qubit® 4.0 fluorometer (Thermo Fisher Scientific) by Equalbit® 1×dsDNA HS Assay Kit (Vazyme) to enable an accurate calculation of the chromatin amount used for immunoprecipitation experiments. Finally, 25 μg chromatin (dsDNA) was immunoprecipitated using 1.25 μg H3K9ac (PTM Biolabs, Hangzhou, China) and H3K9cr (PTM Biolabs), and 150 μg chromatin was immunoprecipitated using 3 μg H3K18la (PTM Biolabs) overnight at 4°C with gentle rotation (20 rpm) in ChIP dilution buffer (1% Triton X-100, 2 mM EDTA, 150 mM NaCl, 50 mM Tri-HCl pH 7.5, 5 mM sodium butyrate and 1× complete proteinase inhibitor). Antibodies-chromatin complexes were then pulled-down using 20 μL Magna ChIP™ protein A+G magnetic beads (Millipore) by incubating with rotation (20 rpm) for 2 h at 4 °C. Beads were washed one time with low salt wash buffer (0.1% SDS, 1% Triton X-100, 2 mM EDTA, 150 mM NaCl and 20 mM Tris-HCl pH 8.1), high salt wash buffer (0.1% SDS, 1% Triton X-100, 2 mM EDTA, 500 mM NaCl and 20 mM Tris-HCl pH 8.1), LiCl wash buffer (250 mM LiCl, 1% NP-40, 10 mM Tris-HCl pH 8.1, 1% sodium deoxycholate and 1 mM EDTA) and two times with TE buffer (1 mM EDTA and 10 mM Tris-HCl pH 8.1) for 10 min each at 4 °C and 30 rpm. Immune complexes were eluted from beads twice for 15 min at 65 °C and 1000 rpm in a thermomixer using 250 μL elution buffer (1% SDS and 100 mM $NaHCO_3$).

The eluted immune complexes were then treated with RNase A (100 μg/ml) for 30 min at 37 °C, and followed by Proteinase K (50 μg/ml) for 2 h at 58 °C and 600 rpm in a thermomixer. Then, the IPed DNA was purified using the phenol-chloroform-isoamyl alcohol (25:24:1) method and precipitated with two volumes of 100% ethanol and 10 ug linear acrylamide (Thermo Fisher Scientific) at -20 °C for 2h. Libraries were then constructed with the TruSeq® ChIP Library Preparation Kit (Illumina) following the manufacturer's instructions and sequenced on an Illumina paired-end platform with 150 bp per read length by Annoroad Gene Technology Co., Ltd.

Sequencing data filtering

The original image data obtained after sequencing was converted into the sequence data stored in FASTQ file format by base calling. Raw reads data were filtered by using Trimmomatic (v.0.36) to remove contaminations and low-quality reads with the parameters "ILLUMINACLIP:Adapter.fa:2:30:10 SLIDINGWINDOW:4:15 LEADING:3 TRAILING:3 MINLEN:36" and quality-controlled using FastQC (v. 0.11.7) [46, 47].

ATAC-seq data analysis

The reads of ATAC-seq data were aligned using Bowtie 2 (v2.4.1) to the mouse reference genome with parameters "-X 1000 --mm --local" [48]. Samtools (v.1.10) was then used to convert files to bam format and filter reads mapped with parameters "-F 1804 -f 2 -q 30" [49]. After removing PCR duplicates using Mark Duplicates function in Picard (v.2.22.0) (http://broadinstitute.github.io/picard/) and mitochondrial reads. MACS2 (v.2.2.7.1) was used to call peaks with parameters "--keep-dup all -q 0.01 -f BAMPE" [50].

ChIP-seq data analysis

High-quality ChIP-seq reads were aligned using Bowtie 2 to the mouse reference genome using default parameters. Then samtools was used to convert files to bam format and filter reads mapped with parameters "-F 1804 -f 2 -q 30". After removing PCR duplicates using Mark Duplicates function in Picard and mitochondrial reads. MACS2 was used to call peaks with parameters "-q 0.01 -f BAMPE" relative to input samples.

RNA-seq data analysis

RNA-seq data were quantified using Salmon (v.1.1.0) with the parameter "-i -g --gcBias --validateMappings" [51]. Differential gene expression analysis was conducted using DESeq2 (v.1.26.0) and differentially expressed genes were defined by p.adjust < 0.05 and absolute fold change more than 0 [52].

Peak annotation and gene enrichment analysis

Peak annotation was performed using ChIPseeker (v.1.22.1) at gene level and the promoter regions was defined as +/- 2 kb of TSS [53]. Genes were considered under regulation of histone marks with at least one peak annotated in their promoter regions or gene body regions. Gene enrichment analysis was performed using clusterProfiler (v3.14.3) [54].

Different binding analysis of ChIP-seq data

For different binding analysis of histone marks in the promoter regions, BEDTools (v2.29.0) "coverage" function was used for read counting within +/- 2 kb of TSS and then DESeq2 was used to perform different binding analysis [55], genes with different binding of histone marks were defined by p.adjust < 0.05 and absolute fold change more than 1.5. DiffBind (v2.14.0) and MAnorm (v1.2.0) were adopted to perform different binding analysis of histone marks in the peak regions, and peaks with different binding of histone marks were defined by p.adjust < 0.05 and absolute fold change more than 1.5 [56, 57].

Sequencing data visualization

Bam files were converted to bigwig files by bamCoverage function of deepTools (v. 3.4.0) with the paramters "--binSize 50 --normalizeUsing RPKM", and "computeMatrix" , "plotHeatmap", "multiBigwigSummary" and "plotCorrelation" functions were used to generate of heatmaps plots [58].

For genome browser representation, data in bigwig files generated by deepTools were visualized using IGV (v. 2.4.10) [59]. BETA “basic” function (--df 0.05 --da 1 -c 0.001) was used for activating and repressive function prediction of peaks with different binding of histone marks [33]. Peaks of replicates were pulled by BEDtools “intersect” function, and bigwig files of replicates were merged by deepTools “bigwigCompare” functions with the parameter “--operation mean”. The mouse reference genome sequence (vM24) and gene annotation (vM24) were downloaded from GENCODE (https://www.gencodegenes.org/). Summary of ChIP-seq, ATAC-seq and RNA-seq data were provided in the S2 Table.

Statistical analysis

All data are expressed as the mean ± SEM. The statistical analysis was analysed by two-tailed unpaired Student’s t test. NS, no significance; p value < 0.05, p value < 0.01 and p value < 0.001 were considered statistically significant (*, **, ***).

Data availability

The ATAC-seq, ChIP-seq and RNA-seq datasets generated and analysed during the current study are available in NCBI's GEO and are accessible through series accession number GSE171088 and GSE171832.

Acknowledgments

This work was supported by the Strategic Priority Research Program of the Chinese Academy of Sciences (Grant No. XDA16010300) and grants from the National Key Research and Development Program of China Project (2016YFA0101402), the National Science Foundation of China (91753140, 81771224).

Author Contributions

Conceptualization and Methodology, S.K.D., and C.M.L.; Investigation, S.K.D., and P.P.L.; Writing-Original Draft, S.K.D.; Writing-Review & Editing, S.K.D., C.M.L., and Z.Q.T.; Supervision, C.M.L.

Competing interests

The authors declare no competing interests.

References

1. Diehl KL, Muir TW. Chromatin as a key consumer in the metabolite economy. Nat Chem Biol. 2020;16(6):620-9. Epub 2020/05/24. doi: 10.1038/s41589-020-0517-x. PubMed PMID: 32444835; PubMed Central PMCID: PMCPMC7258299.
2. Klemm SL, Shipony Z, Greenleaf WJ. Chromatin accessibility and the regulatory epigenome. Nat Rev Genet. 2019;20(4):207-20. Epub 2019/01/25. doi: 10.1038/s41576-018-0089-8. PubMed PMID: 30675018.
3. Li X, Egervari G, Wang Y, Berger SL, Lu Z. Regulation of chromatin and gene expression by metabolic enzymes and metabolites. Nat Rev Mol Cell Biol. 2018;19(9):563-78. Epub 2018/06/23. doi: 10.1038/s41580-018-0029-7. PubMed PMID: 29930302; PubMed Central PMCID: PMCPMC6907087.
4. Sabari BR, Tang Z, Huang H, Yong-Gonzalez V, Molina H, Kong HE, et al. Intracellular crotonyl-CoA stimulates transcription through p300-catalyzed histone crotonylation. Mol Cell. 2015;58(2):203-15. Epub 2015/03/31. doi: 10.1016/j.molcel.2015.02.029. PubMed PMID: 25818647; PubMed Central PMCID: PMCPMC4501262.
5. Zhang D, Tang Z, Huang H, Zhou G, Cui C, Weng Y, et al. Metabolic regulation of gene expression by histone lactylation. Nature. 2019;574(7779):575-80. Epub 2019/10/28. doi: 10.1038/s41586-019-1678-1. PubMed PMID: 31645732; PubMed Central PMCID: PMCPMC6818755.
6. Li K, Wang Z. Histone crotonylation-centric gene regulation. Epigenetics Chromatin. 2021;14(1):10. Epub 2021/02/08. doi: 10.1186/s13072-021-00385-9. PubMed PMID: 33549150; PubMed Central PMCID: PMCPMC7868018.
7. Yu J, Chai P, Xie M, Ge S, Ruan J, Fan X, et al. Histone lactylation drives oncogenesis by facilitating m(6)A reader protein YTHDF2 expression in ocular melanoma. Genome Biol. 2021;22(1):85. Epub 2021/03/18. doi: 10.1186/s13059-021-02308-z. PubMed PMID: 33726814; PubMed Central PMCID: PMCPMC7962360.
8. Li L, Chen K, Wang T, Wu Y, Xing G, Chen M, et al. Glis1 facilitates induction of pluripotency via an epigenome–metabolome–epigenome signalling cascade. Nat Metab. 2020;2(9):882-92.
9. Tan M, Luo H, Lee S, Jin F, Yang JS, Montellier E, et al. Identification of 67 histone marks and histone lysine crotonylation as a new type of histone modification. Cell. 2011;146(6):1016-28. Epub 2011/09/20. doi: 10.1016/j.cell.2011.08.008. PubMed PMID: 21925322; PubMed Central PMCID: PMCPMC3176443.
10. Liu X, Wei W, Liu Y, Yang X, Wu J, Zhang Y, et al. MOF as an evolutionarily conserved histone crotonyltransferase and transcriptional activation by histone acetyltransferase-deficient and crotonyltransferase-competent CBP/p300. Cell Discov. 2017;3(1):17016. Epub 2017/06/06. doi: 10.1038/celldisc.2017.16. PubMed PMID: 28580166; PubMed Central PMCID: PMCPMC5441097.
11. Kollenstart L, de Groot AJL, Janssen GMC, Cheng X, Vreeken K, Martino F, et al. Gcn5 and Esa1 function as histone crotonyltransferases to regulate crotonylation-dependent transcription. J Biol Chem. 2019;294(52):20122-34. Epub 2019/11/09. doi: 10.1074/jbc.RA119.010302. PubMed PMID: 31699900; PubMed Central PMCID: PMCPMC6937567.
12. Kelly RDW, Chandru A, Watson PJ, Song Y, Blades M, Robertson NS, et al. Histone deacetylase (HDAC) 1 and 2 complexes regulate both histone acetylation and crotonylation in vivo. Sci Rep. 2018;8(1):14690. Epub 2018/10/04. doi: 10.1038/s41598-018-32927-9. PubMed PMID: 30279482; PubMed Central PMCID: PMCPMC6168483.
13. Wei W, Liu X, Chen J, Gao S, Lu L, Zhang H, et al. Class I histone deacetylases are major histone decrotonylases: evidence for critical and broad function of histone crotonylation in transcription. Cell Res. 2017;27(7):898-915. Epub 2017/05/13. doi: 10.1038/cr.2017.68. PubMed PMID: 28497810; PubMed Central PMCID: PMCPMC5518989.
14. Fellows R, Denizot J, Stellato C, Cuomo A, Jain P, Stoyanova E, et al. Microbiota derived short chain fatty acids promote histone crotonylation in the colon through histone deacetylases. Nat Commun. 2018;9(1):105. doi: 10.1038/s41467-017-02651-5. PubMed PMID: WOS:000419658100005.
15. Li Y, Sabari BR, Panchenko T, Wen H, Zhao D, Guan H, et al. Molecular Coupling of Histone Crotonylation and Active Transcription by AF9 YEATS Domain. Mol Cell. 2016;62(2):181-93. Epub

517 2016/04/23. doi: 10.1016/j.molcel.2016.03.028. PubMed PMID: 27105114; PubMed Central PMCID:
518 PMCPMC4841940.
519 16. Zhao D, Guan H, Zhao S, Mi W, Wen H, Li Y, et al. YEATS2 is a selective histone crotonylation
520 reader. Cell Res. 2016;26(5):629-32. Epub 2016/04/23. doi: 10.1038/cr.2016.49. PubMed PMID:
521 27103431; PubMed Central PMCID: PMCPMC4856769.
522 17. Andrews FH, Shinsky SA, Shanle EK, Bridgers JB, Gest A, Tsun IK, et al. The Taf14 YEATS
523 domain is a reader of histone crotonylation. Nat Chem Biol. 2016;12(6):396-8. Epub 2016/04/19. doi:
524 10.1038/nchembio.2065. PubMed PMID: 27089029; PubMed Central PMCID: PMCPMC4871749.
525 18. Xiong X, Panchenko T, Yang S, Zhao S, Yan P, Zhang W, et al. Selective recognition of histone
526 crotonylation by double PHD fingers of MOZ and DPF2. Nat Chem Biol. 2016;12(12):1111-8. Epub
527 2016/10/25. doi: 10.1038/nchembio.2218. PubMed PMID: 27775714; PubMed Central PMCID:
528 PMCPMC5253430.
529 19. Liu S, Yu H, Liu Y, Liu X, Zhang Y, Bu C, et al. Chromodomain Protein CDYL Acts as a Crotonyl-
530 CoA Hydratase to Regulate Histone Crotonylation and Spermatogenesis. Mol Cell. 2017;67(5):853-66
531 e5. Epub 2017/08/15. doi: 10.1016/j.molcel.2017.07.011. PubMed PMID: 28803779.
532 20. Fang Y, Xu X, Ding J, Yang L, Doan MT, Karmaus PWF, et al. Histone crotonylation promotes
533 mesoendodermal commitment of human embryonic stem cells. Cell Stem Cell. 2021;28(4):748-63 e7.
534 Epub 2021/01/16. doi: 10.1016/j.stem.2020.12.009. PubMed PMID: 33450185; PubMed Central
535 PMCID: PMCPMC8026719.
536 21. Tang X, Chen XF, Sun X, Xu P, Zhao X, Tong Y, et al. Short-Chain Enoyl-CoA Hydratase
537 Mediates Histone Crotonylation and Contributes to Cardiac Homeostasis. Circulation.
538 2021;143(10):1066-9. Epub 2021/03/09. doi: 10.1161/CIRCULATIONAHA.120.049438. PubMed PMID:
539 33683949.
540 22. Jiang G, Nguyen D, Archin NM, Yukl SA, Mendez-Lagares G, Tang Y, et al. HIV latency is
541 reversed by ACSS2-driven histone crotonylation. J Clin Invest. 2018;128(3):1190-8. Epub 2018/02/20.
542 doi: 10.1172/JCI98071. PubMed PMID: 29457784; PubMed Central PMCID: PMCPMC5824862.
543 23. Liu Y, Li M, Fan M, Song Y, Yu H, Zhi X, et al. Chromodomain Y-like protein–mediated histone
544 crotonylation regulates stress-induced depressive behaviors. Biol Psychiatry. 2019;85(8):635-49.
545 24. Li Y, Wen H, Xi Y, Tanaka K, Wang H, Peng D, et al. AF9 YEATS domain links histone
546 acetylation to DOT1L-mediated H3K79 methylation. Cell. 2014;159(3):558-71. Epub 2014/11/25. doi:
547 10.1016/j.cell.2014.09.049. PubMed PMID: 25417107; PubMed Central PMCID: PMCPMC4344132.
548 25. Luo Z, Lin C, Shilatifard A. The super elongation complex (SEC) family in transcriptional
549 control. Nat Rev Mol Cell Biol. 2012;13(9):543-7. Epub 2012/08/17. doi: 10.1038/nrm3417. PubMed
550 PMID: 22895430.
551 26. Gowans GJ, Bridgers JB, Zhang J, Dronamraju R, Burnetti A, King DA, et al. Recognition of
552 Histone Crotonylation by Taf14 Links Metabolic State to Gene Expression. Mol Cell. 2019;76(6):909-
553 21 e3. Epub 2019/11/05. doi: 10.1016/j.molcel.2019.09.029. PubMed PMID: 31676231; PubMed
554 Central PMCID: PMCPMC6931132.
555 27. Crespo M, Damont A, Blanco M, Lastrucci E, El Kennani S, Ialy-Radio C, et al. Multi-omic
556 analysis of gametogenesis reveals a novel signature at the promoters and distal enhancers of active
557 genes. Nucleic Acids Res. 2020;48(8):4115-38. doi: 10.1093/nar/gkaa163. PubMed PMID:
558 WOS:000569096800015.
559 28. Lu Y, Xu Q, Liu Y, Yu Y, Cheng ZY, Zhao Y, et al. Dynamics and functional interplay of histone
560 lysine butyrylation, crotonylation, and acetylation in rice under starvation and submergence.
561 Genome Biol. 2018;19(1):144. Epub 2018/09/27. doi: 10.1186/s13059-018-1533-y. PubMed PMID:
562 30253806; PubMed Central PMCID: PMCPMC6154804.
563 29. Wang J, Weaver IC, Gauthier-Fisher A, Wang H, He L, Yeomans J, et al. CBP histone
564 acetyltransferase activity regulates embryonic neural differentiation in the normal and Rubinstein-
565 Taybi syndrome brain. Dev Cell. 2010;18(1):114-25. Epub 2010/02/16. doi:
566 10.1016/j.devcel.2009.10.023. PubMed PMID: 20152182.

30. Tang T, Zhang Y, Wang Y, Cai Z, Lu Z, Li L, et al. HDAC1 and HDAC2 Regulate Intermediate Progenitor Positioning to Safeguard Neocortical Development. Neuron. 2019;101(6):1117-33 e5. Epub 2019/02/03. doi: 10.1016/j.neuron.2019.01.007. PubMed PMID: 30709655.
31. Yao B, Christian KM, He C, Jin P, Ming GL, Song H. Epigenetic mechanisms in neurogenesis. Nat Rev Neurosci. 2016;17(9):537-49. Epub 2016/06/24. doi: 10.1038/nrn.2016.70. PubMed PMID: 27334043; PubMed Central PMCID: PMCPMC5610421.
32. Marzluff WF, Koreski KP. Birth and Death of Histone mRNAs. Trends Genet. 2017;33(10):745-59. Epub 2017/09/05. doi: 10.1016/j.tig.2017.07.014. PubMed PMID: 28867047; PubMed Central PMCID: PMCPMC5645032.
33. Wang S, Sun H, Ma J, Zang C, Wang C, Wang J, et al. Target analysis by integration of transcriptome and ChIP-seq data with BETA. Nat Protoc. 2013;8(12):2502-15. Epub 2013/11/23. doi: 10.1038/nprot.2013.150. PubMed PMID: 24263090; PubMed Central PMCID: PMCPMC4135175.
34. Martin BJE, Brind'Amour J, Kuzmin A, Jensen KN, Liu ZC, Lorincz M, et al. Transcription shapes genome-wide histone acetylation patterns. Nat Commun. 2021;12(1):210. Epub 2021/01/13. doi: 10.1038/s41467-020-20543-z. PubMed PMID: 33431884; PubMed Central PMCID: PMCPMC7801501.
35. Bensaude O. Inhibiting eukaryotic transcription. Which compound to choose? How to evaluate its activity? Which compound to choose? How to evaluate its activity? Transcription. 2011;2(3):103-8.
36. Wissink EM, Vihervaara A, Tippens ND, Lis JT. Nascent RNA analyses: tracking transcription and its regulation. Nat Rev Genet. 2019;20(12):705-23. Epub 2019/08/11. doi: 10.1038/s41576-019-0159-6. PubMed PMID: 31399713; PubMed Central PMCID: PMCPMC6858503.
37. Huang H, Zhang D, Wang Y, Perez-Neut M, Han Z, Zheng YG, et al. Lysine benzoylation is a histone mark regulated by SIRT2. Nat Commun. 2018;9(1):3374. Epub 2018/08/30. doi: 10.1038/s41467-018-05567-w. PubMed PMID: 30154464; PubMed Central PMCID: PMCPMC6113264.
38. Khacho M, Harris R, Slack RS. Mitochondria as central regulators of neural stem cell fate and cognitive function. Nature Reviews Neuroscience. 2019;20(1):34-48. doi: 10.1038/s41583-018-0091-3. PubMed PMID: WOS:000453242600007.
39. Lipinski M, Munoz-Viana R, Del Blanco B, Marquez-Galera A, Medrano-Relinque J, Carames JM, et al. KAT3-dependent acetylation of cell type-specific genes maintains neuronal identity in the adult mouse brain. Nat Commun. 2020;11(1):2588. Epub 2020/05/24. doi: 10.1038/s41467-020-16246-0. PubMed PMID: 32444594; PubMed Central PMCID: PMCPMC7244750.
40. Liu J, Wu X, Zhang H, Pfeifer GP, Lu Q. Dynamics of RNA Polymerase II Pausing and Bivalent Histone H3 Methylation during Neuronal Differentiation in Brain Development. Cell Rep. 2017;20(6):1307-18. Epub 2017/08/10. doi: 10.1016/j.celrep.2017.07.046. PubMed PMID: 28793256; PubMed Central PMCID: PMCPMC5564459.
41. Wang Z, Zang C, Cui K, Schones DE, Barski A, Peng W, et al. Genome-wide mapping of HATs and HDACs reveals distinct functions in active and inactive genes. Cell. 2009;138(5):1019-31. Epub 2009/08/25. doi: 10.1016/j.cell.2009.06.049. PubMed PMID: 19698979; PubMed Central PMCID: PMCPMC2750862.
42. Vaid R, Wen J, Mannervik M. Release of promoter–proximal paused Pol II in response to histone deacetylase inhibition. Nucleic Acids Res. 2020;48(9):4877-90.
43. Huang H, Zhang D, Weng Y, Delaney K, Tang Z, Yan C, et al. The regulatory enzymes and protein substrates for the lysine β-hydroxybutyrylation pathway. Sci Adv. 2021;7(9):eabe2771.
44. Moreno-Yruela C, Zhang D, Wei W, Baek M, Gao J, Nielsen AL, et al. Class I Histone Deacetylases (HDAC1⍰3) are Histone Lysine Delactylases. bioRxiv. 2021.
45. Shechter D, Dormann HL, Allis CD, Hake SB. Extraction, purification and analysis of histones. Nat Protoc. 2007;2(6):1445-57. Epub 2007/06/05. doi: 10.1038/nprot.2007.202. PubMed PMID: 17545981.

617 46. Bolger AM, Lohse M, Usadel B. Trimmomatic: a flexible trimmer for Illumina sequence data.
618 Bioinformatics. 2014;30(15):2114-20. Epub 2014/04/04. doi: 10.1093/bioinformatics/btu170.
619 PubMed PMID: 24695404; PubMed Central PMCID: PMCPMC4103590.
620 47. Andrews S. FastQC: a quality control tool for high throughput sequence data. Babraham
621 Bioinformatics, Babraham Institute, Cambridge, United Kingdom; 2010.
622 48. Langmead B, Salzberg SL. Fast gapped-read alignment with Bowtie 2. Nat Methods.
623 2012;9(4):357-9. Epub 2012/03/06. doi: 10.1038/nmeth.1923. PubMed PMID: 22388286; PubMed
624 Central PMCID: PMCPMC3322381.
625 49. Li H, Handsaker B, Wysoker A, Fennell T, Ruan J, Homer N, et al. The Sequence
626 Alignment/Map format and SAMtools. Bioinformatics. 2009;25(16):2078-9. Epub 2009/06/10. doi:
627 10.1093/bioinformatics/btp352. PubMed PMID: 19505943; PubMed Central PMCID:
628 PMCPMC2723002.
629 50. Feng J, Liu T, Qin B, Zhang Y, Liu XS. Identifying ChIP-seq enrichment using MACS. Nat Protoc.
630 2012;7(9):1728-40. Epub 2012/09/01. doi: 10.1038/nprot.2012.101. PubMed PMID: 22936215;
631 PubMed Central PMCID: PMCPMC3868217.
632 51. Patro R, Duggal G, Love MI, Irizarry RA, Kingsford C. Salmon provides fast and bias-aware
633 quantification of transcript expression. Nat Methods. 2017;14(4):417-9. Epub 2017/03/07. doi:
634 10.1038/nmeth.4197. PubMed PMID: 28263959; PubMed Central PMCID: PMCPMC5600148.
635 52. Love MI, Huber W, Anders S. Moderated estimation of fold change and dispersion for RNA-
636 seq data with DESeq2. Genome Biol. 2014;15(12):550. Epub 2014/12/18. doi: 10.1186/s13059-014-
637 0550-8. PubMed PMID: 25516281; PubMed Central PMCID: PMCPMC4302049.
638 53. Yu G, Wang LG, He QY. ChIPseeker: an R/Bioconductor package for ChIP peak annotation,
639 comparison and visualization. Bioinformatics. 2015;31(14):2382-3. Epub 2015/03/15. doi:
640 10.1093/bioinformatics/btv145. PubMed PMID: 25765347.
641 54. Yu G, Wang LG, Han Y, He QY. clusterProfiler: an R package for comparing biological themes
642 among gene clusters. OMICS. 2012;16(5):284-7. Epub 2012/03/30. doi: 10.1089/omi.2011.0118.
643 PubMed PMID: 22455463; PubMed Central PMCID: PMCPMC3339379.
644 55. Quinlan AR, Hall IM. BEDTools: a flexible suite of utilities for comparing genomic features.
645 Bioinformatics. 2010;26(6):841-2. Epub 2010/01/30. doi: 10.1093/bioinformatics/btq033. PubMed
646 PMID: 20110278; PubMed Central PMCID: PMCPMC2832824.
647 56. Shao Z, Zhang Y, Yuan GC, Orkin SH, Waxman DJ. MAnorm: a robust model for quantitative
648 comparison of ChIP-Seq data sets. Genome Biol. 2012;13(3):R16. Epub 2012/03/20. doi: 10.1186/gb-
649 2012-13-3-r16. PubMed PMID: 22424423; PubMed Central PMCID: PMCPMC3439967.
650 57. Stark R, Brown GJRpv. DiffBind: differential binding analysis of ChIP-Seq peak data. R
651 package version. 2011;100(4.3).
652 58. Ramirez F, Ryan DP, Gruning B, Bhardwaj V, Kilpert F, Richter AS, et al. deepTools2: a next
653 generation web server for deep-sequencing data analysis. Nucleic Acids Res. 2016;44(W1):W160-W5.
654 doi: 10.1093/nar/gkw257. PubMed PMID: WOS:000379786800027.
655 59. Thorvaldsdottir H, Robinson JT, Mesirov JP. Integrative Genomics Viewer (IGV): high-
656 performance genomics data visualization and exploration. Brief Bioinform. 2013;14(2):178-92. Epub
657 2012/04/21. doi: 10.1093/bib/bbs017. PubMed PMID: 22517427; PubMed Central PMCID:
658 PMCPMC3603213.

659

660

Figures and figure legends

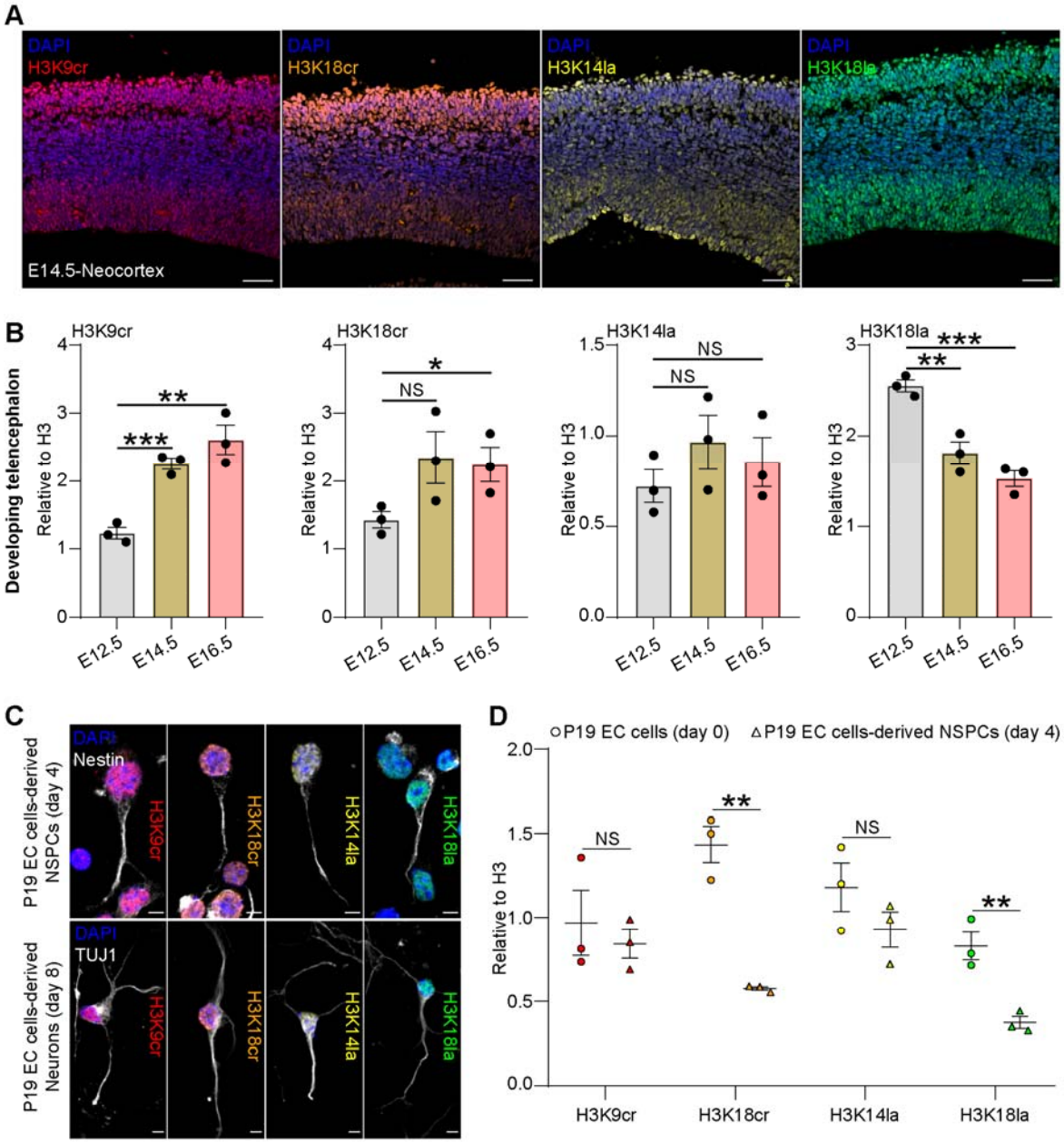

Fig 1. Existence and changes of histone Kcr and Kla during neural development. (**A**) Immunostaining of indicated histone marks on mouse forebrain sections at E14.5 (n = 1). Scale bar, 50 μm. (**B**) Statical analysis for changes of indicated histone marks in the developing telencephalon by western blot assay (n = 3). (**C**) Immunocytochemistry of indicated histone marks and markers for P19 EC cells-derived NSPCs (Nestin) and neurons (TUJ1) (n = 1). Scale bar, 5 μm. (**D**) Statical analysis for changes of indicated histone marks during neural differentiation of P19 EC cells (n = 3). Data are represented as mean ± SEM. NS, no significance; *P< 0.05, **P< 0.01, ***P< 0.001 by two-tailed unpaired Student's t-test in (B and D). See also S1 Fig.

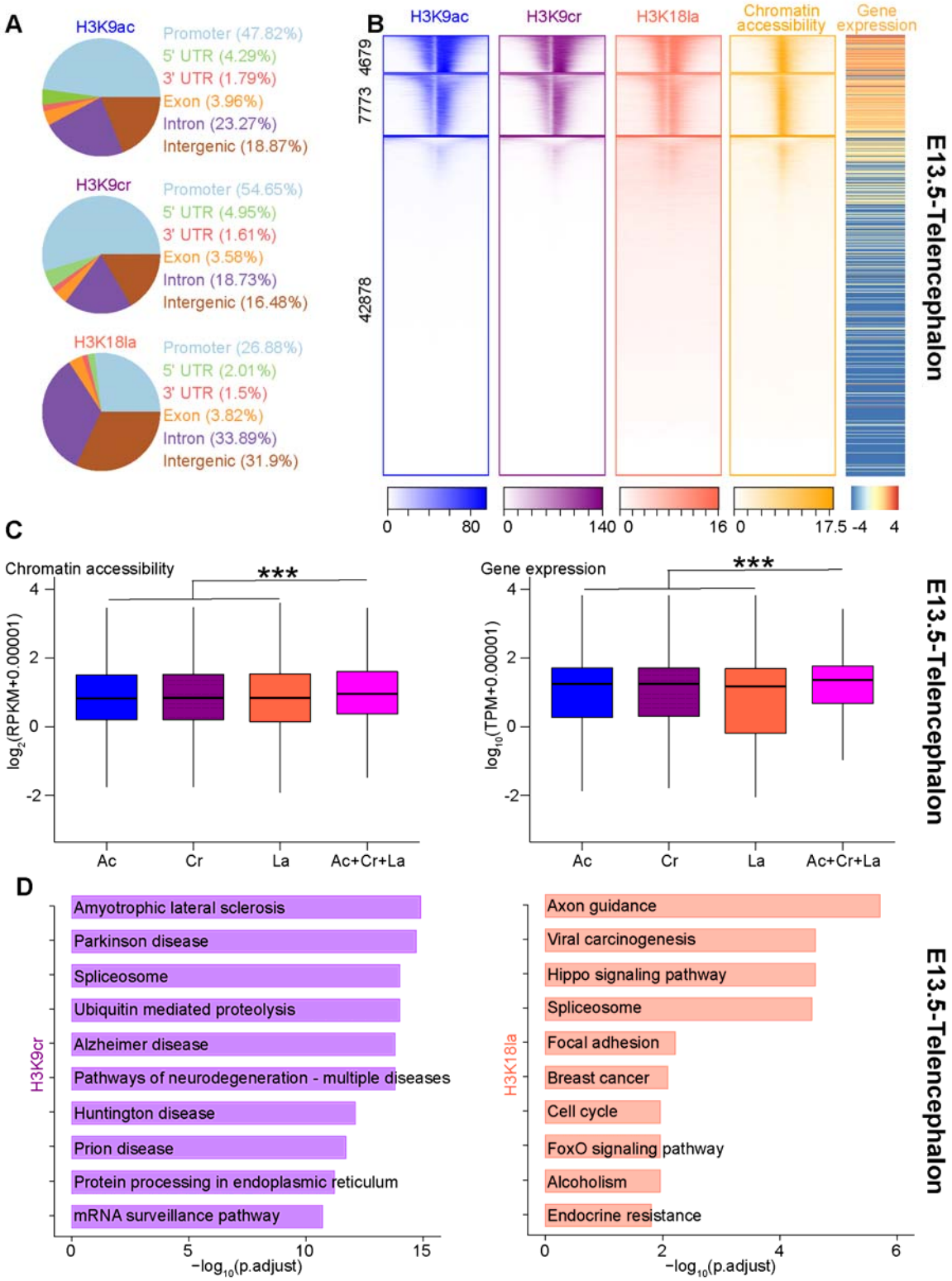

Fig 2. Multi-omics profiling and functional annotation of H3K9cr and H3K18la in vivo. (**A**) Pie chart showing distribution of peaks of indicated histone marks at annotated genomic regions in the E13.5 telencephalon. (**B**) Heatmaps of indicated histone marks intensity (scaled by RPKM), chromatin accessibility levels (scaled by RPKM) plotted within +/- 2.5 kb of the TSS (5' to 3'), and

gene expression levels (scaled by $\log_{10}$(TPM+0.00001)) which were divided to into three clusters and ranked from the highest to the lowest by H3K9ac signal in the E13.5 telencephalon, the number of genes in each cluster was labelled on the left. (**C**) Boxplot showing comparison of changes of chromatin accessibility (left panel) and gene expression (right panel) across different groups of genes in the E13.5 telencephalon. Ac, Cr, La and Ac+Cr+La: genes under regulation of H3K9ac (13789 genes), H3K9cr (13726 genes), H3K18la (13113 genes) and all three marks (10162 genes) respectively. (**D**) KEGG pathway enrichment analysis of genes with the strongest H3K9cr signal (left panel, 3561 genes) and H3K18la signal (right panel, 3568 genes) in the E13.5 telencephalon. ***$P < 0.001$ by two-tailed unpaired Student's t-test in (C). See also S2-S4 Figs.

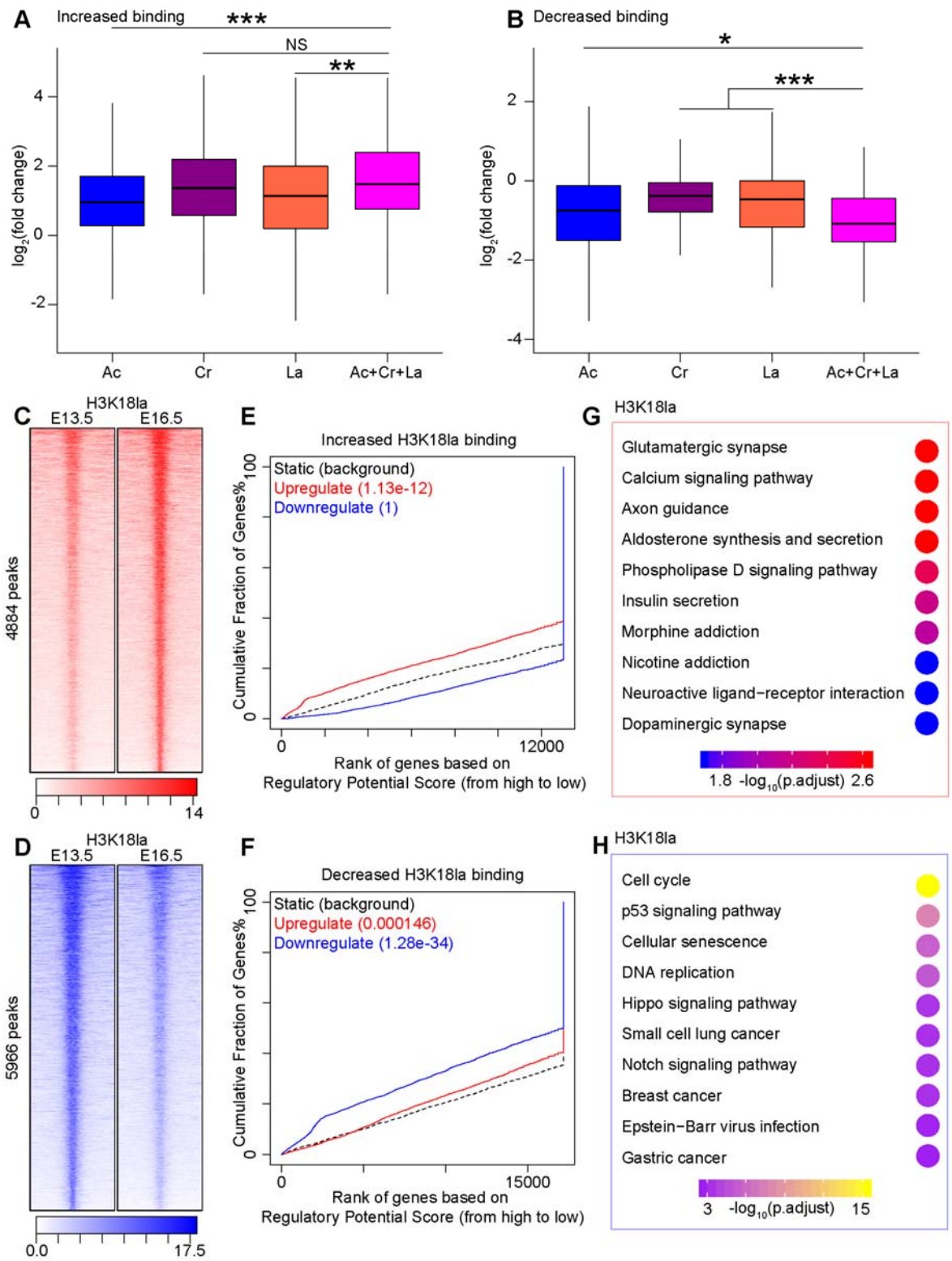

Fig 3. Genome-wide dynamic changes of H3K18la during neural development. (**A**) Boxplot showing comparison of gene expression changes with increased binding of indicated histone marks in the promoter regions across different groups of genes. Ac, Cr, La and Ac+Cr+La: genes with increased binding of H3K9ac (3717 genes), H3K9cr (1785 genes), H3K18la (542 genes) and all three

marks (196 genes) respectively. (**B**) Boxplot showing comparison of gene expression changes with decreased binding of indicated histone marks in the promoter regions across different groups of genes. Ac, Cr, La and Ac+Cr+La: genes with decreased binding of H3K9ac (784 genes), H3K9cr (2693 genes), H3K18la (730 genes) and all three marks (178 genes) respectively. (**C and D**) Heatmaps at peaks with increased (C) and decreased (D) H3K18la binding (scaled by RPKM) plotted within +/- 5 kb of the peak center (5' to 3'), the number of peaks was labelled on the left. **(E and F)** BETA plot of combined computational analysis of H3K18la ChIP-seq and RNA-seq data using peaks with increased (E) and decreased (F) H3K18la binding respectively. (**G and H**) KEGG pathway enrichment analysis of up-regulated genes with increased H3K18la binding (G) and down-regulated genes with decreased H3K18la binding (H), there were 411 and 557 genes in (G) and (H) respectively. NS, no significance; *****P< 0.05, ******P< 0.01, *******P< 0.001 by two-tailed unpaired Student's t-test in (A and B). See also S5-S8 Figs.

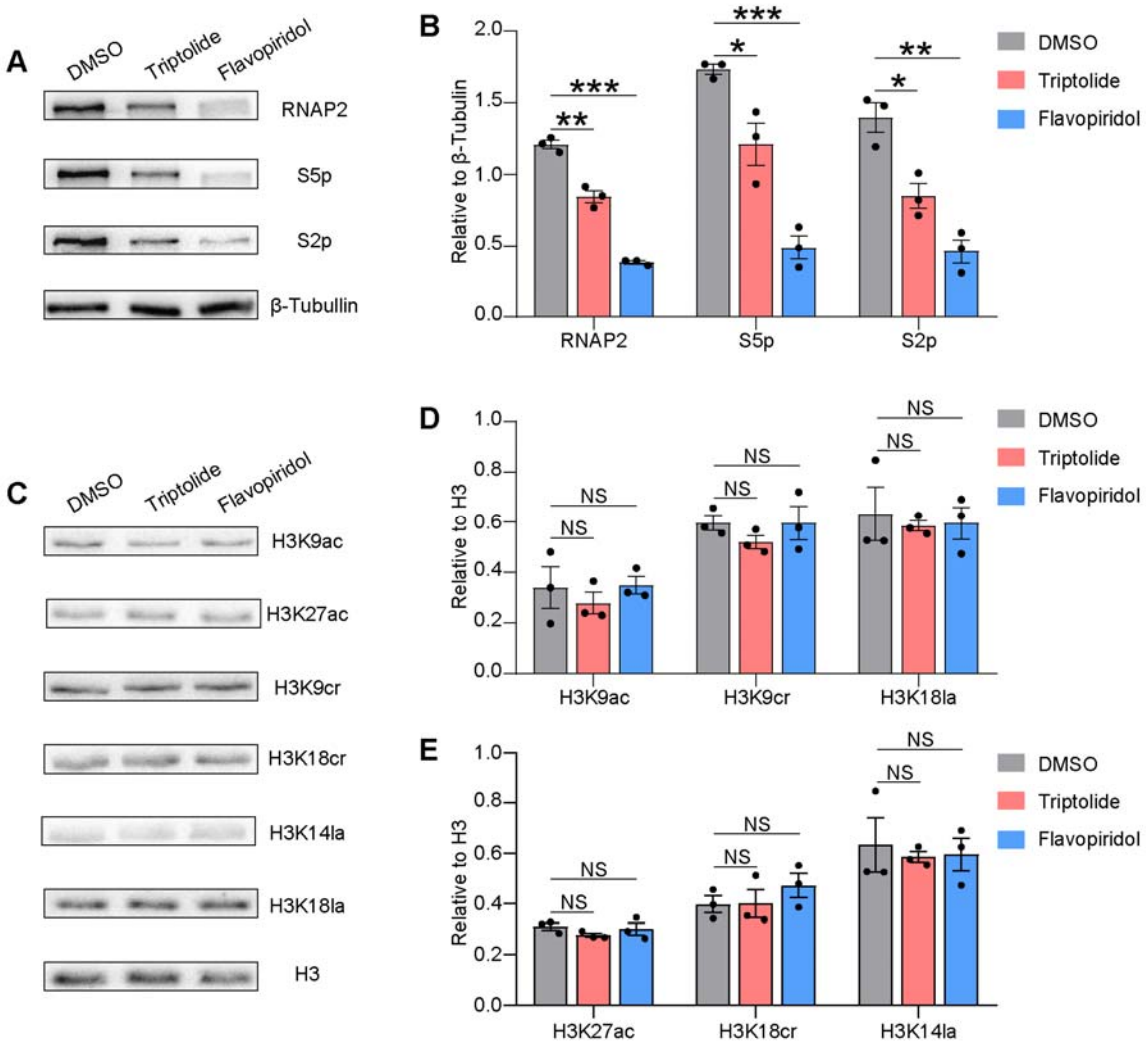

Fig 4. The association between transcription inhibition and histone Kcr and Kla levels. (**A and B**) A representative plot (A) and quantification analysis (B) of changes of RNA polymerase II (RNAP2), RNAP2 serine 5 CTD phosphorylation (S5p) and RNAP2 serine 2 CTD phosphorylation (S2p) levels in P19 EC cells-derived NSPCs treated with DMSO, Triptolide and Flavopiridol respectively (n = 3). (**C-E**) A representative plot (C) and quantification analysis (D and E) of changes of H3K9ac, H3K27ac, H3K9cr, H3K18cr, H3K14la and H3K18la levels in P19 EC cells-derived NSPCs treated with DMSO, Triptolide and Flavopiridol respectively (n = 3). Data are represented as mean ± SEM. NS, no significance; *P< 0.05, **P< 0.01, ***P< 0.001 by two-tailed unpaired Student's t-test in (B, D and E).

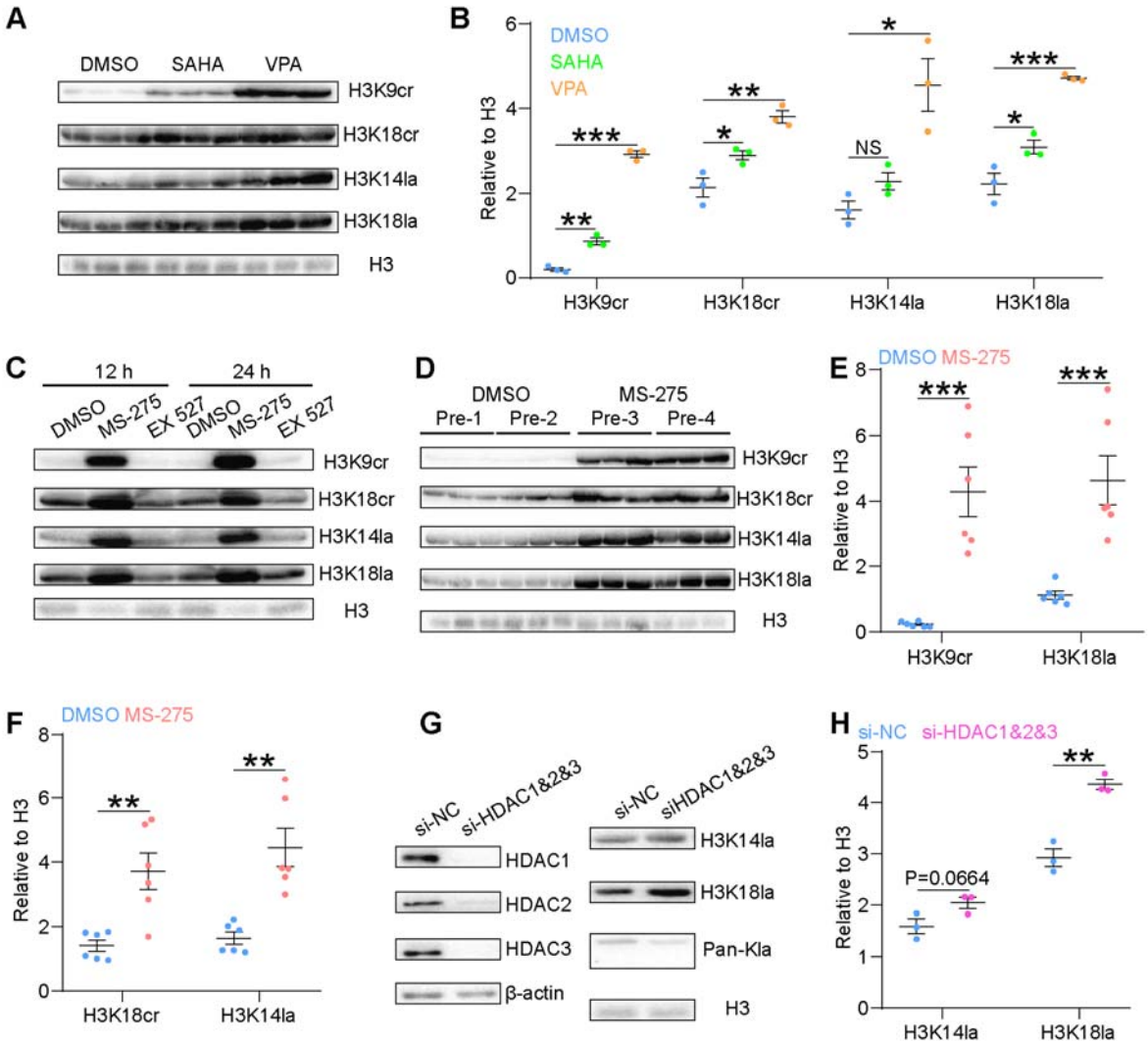

Fig 5. HDAC1-3 inhibition stimulates histone Kcr and Kla levels. (**A and B**) A representative plot (A) and quantification analysis (B) of changes of indicated histone marks in DMSO, SAHA and VPA treated P19 EC cells (n = 3). (**C**) Western blot assay of changes of indicated histone marks in DMSO, MS-275 and EX 527 treated P19 EC cells for different time intervals (n = 1). (**D-F**) Western blot assay (D) and quantification analysis (E and F) of changes of indicated histone marks in the telencephalon at E15.5 injected with DMSO or MS-275 for two consecutive days (E13.5-E15.5). (**G**) A representative plot showing efficient knockdown of *Hdac1-3* (left panel) and changes of histone Kla levels (right panel) in P19 EC cells. (**H**) Quantification analysis of changes of H3K14la and H3K18la levels after *Hdac*1-3 knockdown in P19 EC cells (n = 3). Data are represented as mean ± SEM. NS, no significance; *P< 0.05, **P< 0.01, ***P< 0.001 by two-tailed unpaired Student's t-test in (B, E, F and H). Pre: pregnant mice.

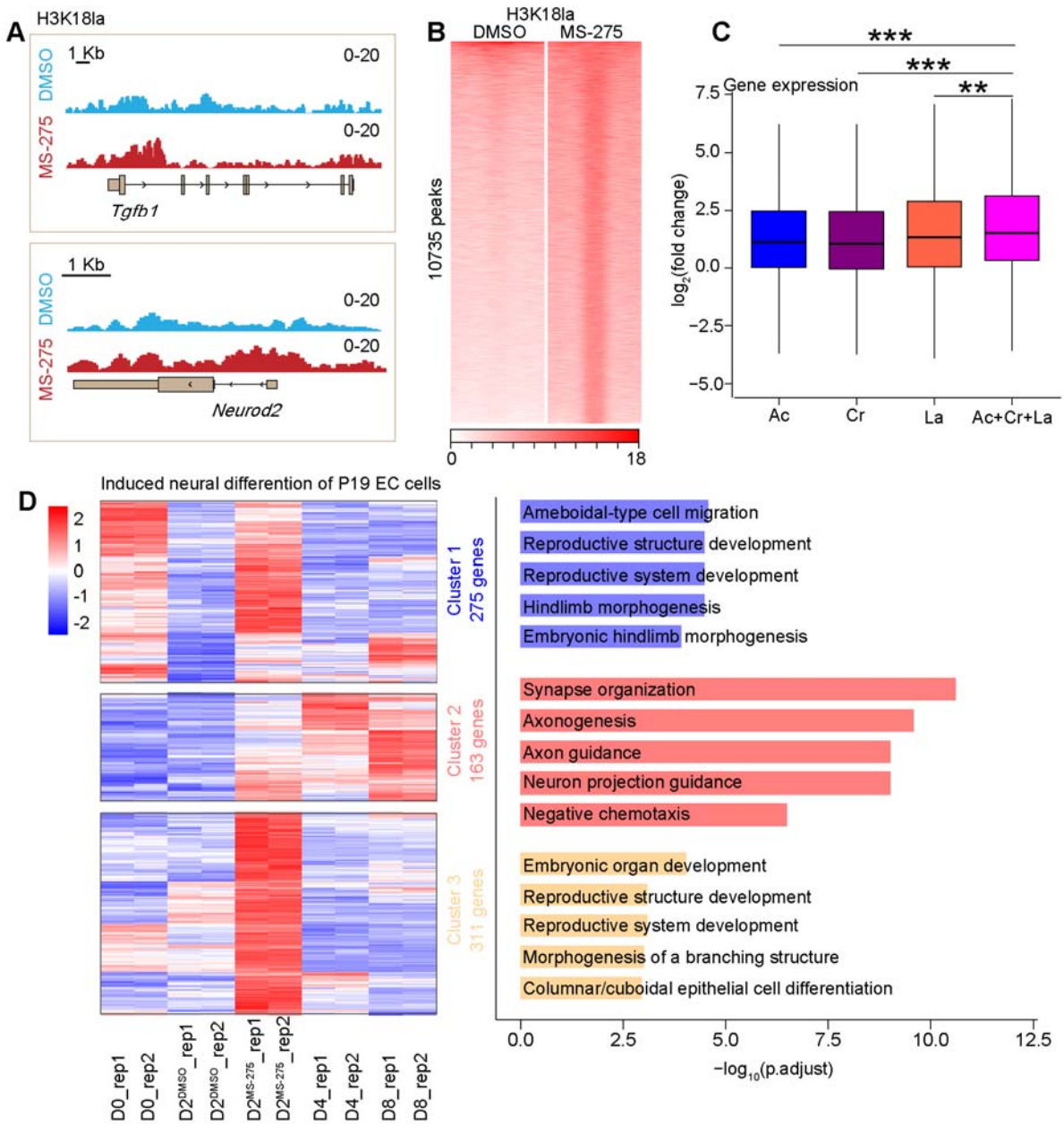

Fig 6. MS-275 regulates cell fate determination via H3K18la. (**A**) Representative genome-browser view at *Tgfb1 and Neuord2* gene of different sequencing data sets. (**B**) Heatmaps at peaks with increased H3K18la binding (scaled by RPKM) plotted within +/- 1 kb of the peak center (5' to 3'), the number of peaks was labelled on the left. (**C**) Boxplot showing comparison of gene expression changes with increased indicated histone marks binding in the promoter regions across different groups of genes. Ac, Cr, La and Ac+Cr+La: genes with increased binding of H3K9ac (4883 genes), H3K9cr (4757 genes), H3K18la (1197 genes) and all three marks (744 genes) respectively. (**D**) Heatmap showing dynamic changes of up-regulated genes (DESeq2 vsd-normalized RNA-seq counts and scaled by row) with increased H3K18la binding after MS-275 treatment during neural differentiation process of P19 EC cells, and these genes were divided into three clusters according

their expression patterns (left panel), with the results of GO enrichment analysis (biological process) of genes in each cluster on right panel. **P< 0.01, ***P< 0.001 by two-tailed unpaired Student's t-test in (C). See also S9 Fig.

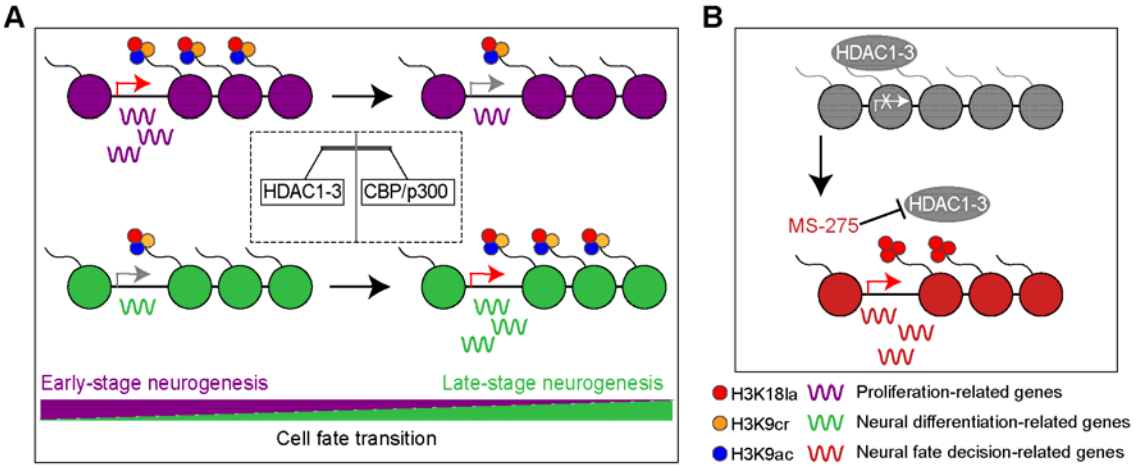

Fig 7. A proposed working model of histone lysine acylations to regulate gene expression and cell fate transition during neural development.

Supporting information for

Dynamic profiling and functional interpretation of histone lysine crotonylation and lactylation during neural development

Shang-Kun Dai[1,2,3], Pei-Pei Liu[1,3], Zhao-Qian Teng[1,2,3], and Chang-Mei Liu[1,2,3,4,*]

[1]State Key Laboratory of Stem Cell and Reproductive Biology, Institute of Zoology, Chinese Academy of Sciences, Beijing 100101, China.

[2]Savaid Medical School, University of Chinese Academy of Sciences, Beijing 100049, China.

[3]Institute for Stem Cell and Regeneration, Chinese Academy of Sciences, Beijing 100101, China.

*Corresponding author. Tel: +86-10-82619690; Email: liuchm@ioz.ac.cn

Running title: Characterization of histone lysine acylations during neural development

Keywords: Histone lysine crotonylation, histone lysine lactylation, transcriptional regulation, neural development, histone deacetylases

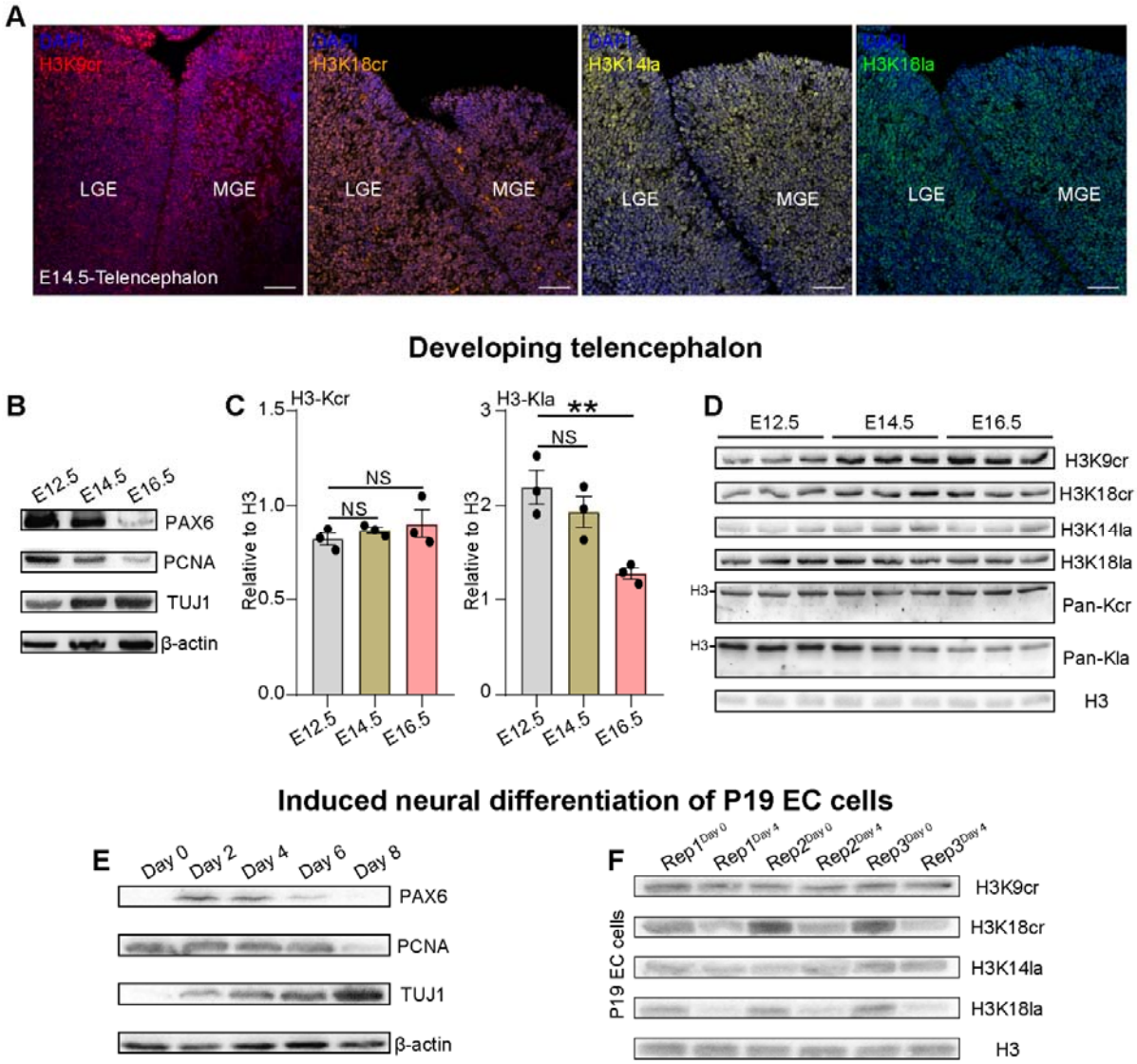

S1 Fig. Dynamic changes of histone Kcr and Kla in vivo and in cells. (**A**) Immunostaining of indicated histone marks on mouse forebrain sections at E14.5 (n = 1), LGE: lateral ganglionic eminence and MGE: ganglionic eminence. Scale bar, 50 μm. (**B**) Western blot assay of PAX6, PCNA and TUJ1 expression in different development stages of telencephalon, which indicated robust neurogenesis (n = 1). (**C**) Statical analysis for changes of H3-Kcr and H3-Kla levels in the developing telencephalon by western blot assay (n = 3). (**D**) Original images of western blot assay of indicated histone marks in the developing telencephalon (n = 3). (**E**) Western blot assay of PAX6, PCNA and TUJ1 expression across various time points of RA-induced neural differentiation of P19 EC cells, which demonstrated successfully induced neural differentiation of P19 EC cells (n = 1). (F) Original images of western blot assay of indicated histone marks in P19 EC cells-derived day 4 NSPCs and day 8 neurons (n = 3). Data are represented as mean ± SEM. NS, no significance; **P< 0.01 by two-tailed unpaired Student's t-test in (C). Related to Fig 1.

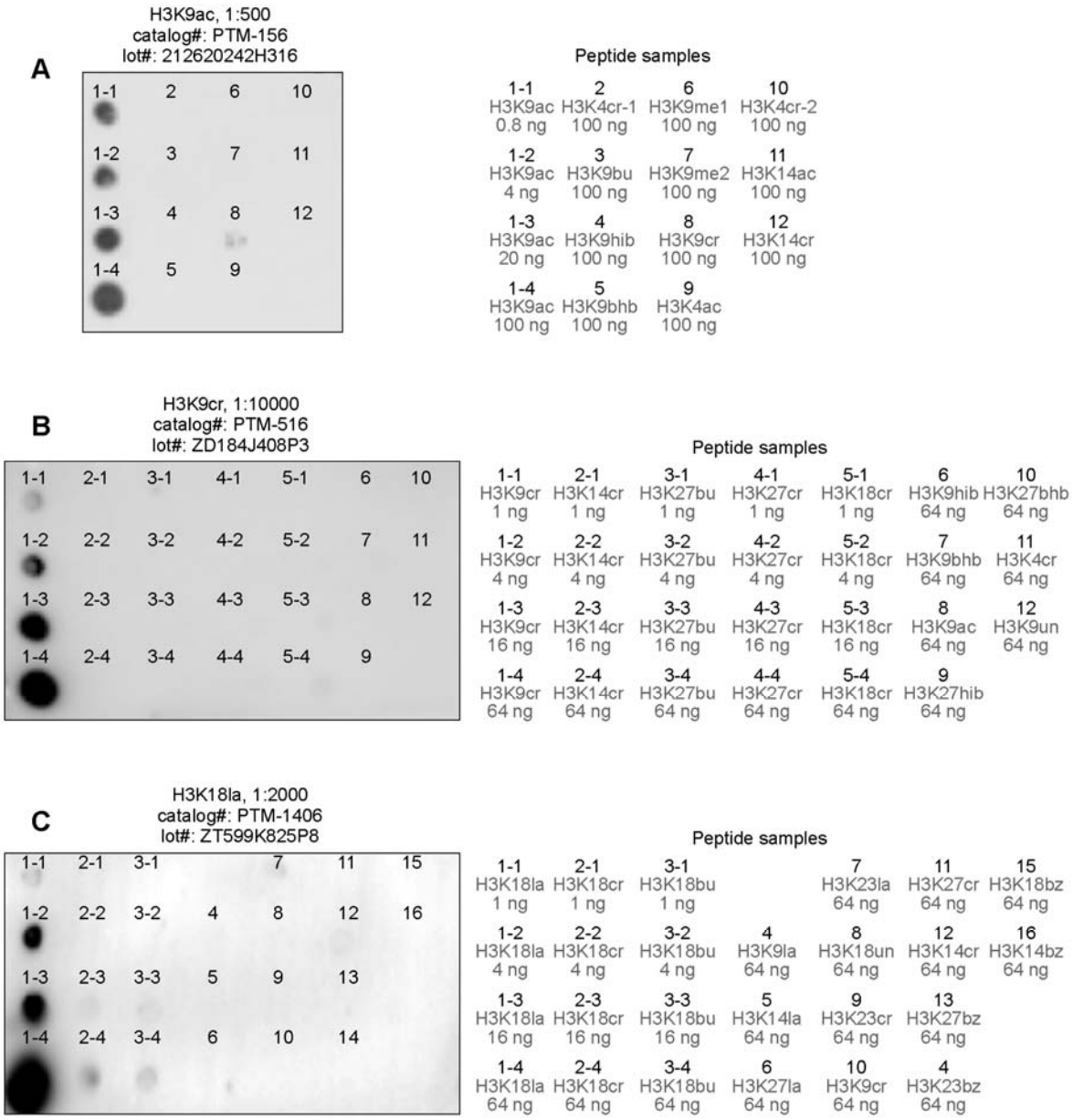

S2 Fig. Dot blot assay of antibodies used in ChIP-seq. (**A-C**) Dot blot assay of H3K9ac (A), H3K9cr (B) and H3K18la (C) antibodies demonstrating its specificity, and the peptide samples used were listed on the right. Related to Fig 2.

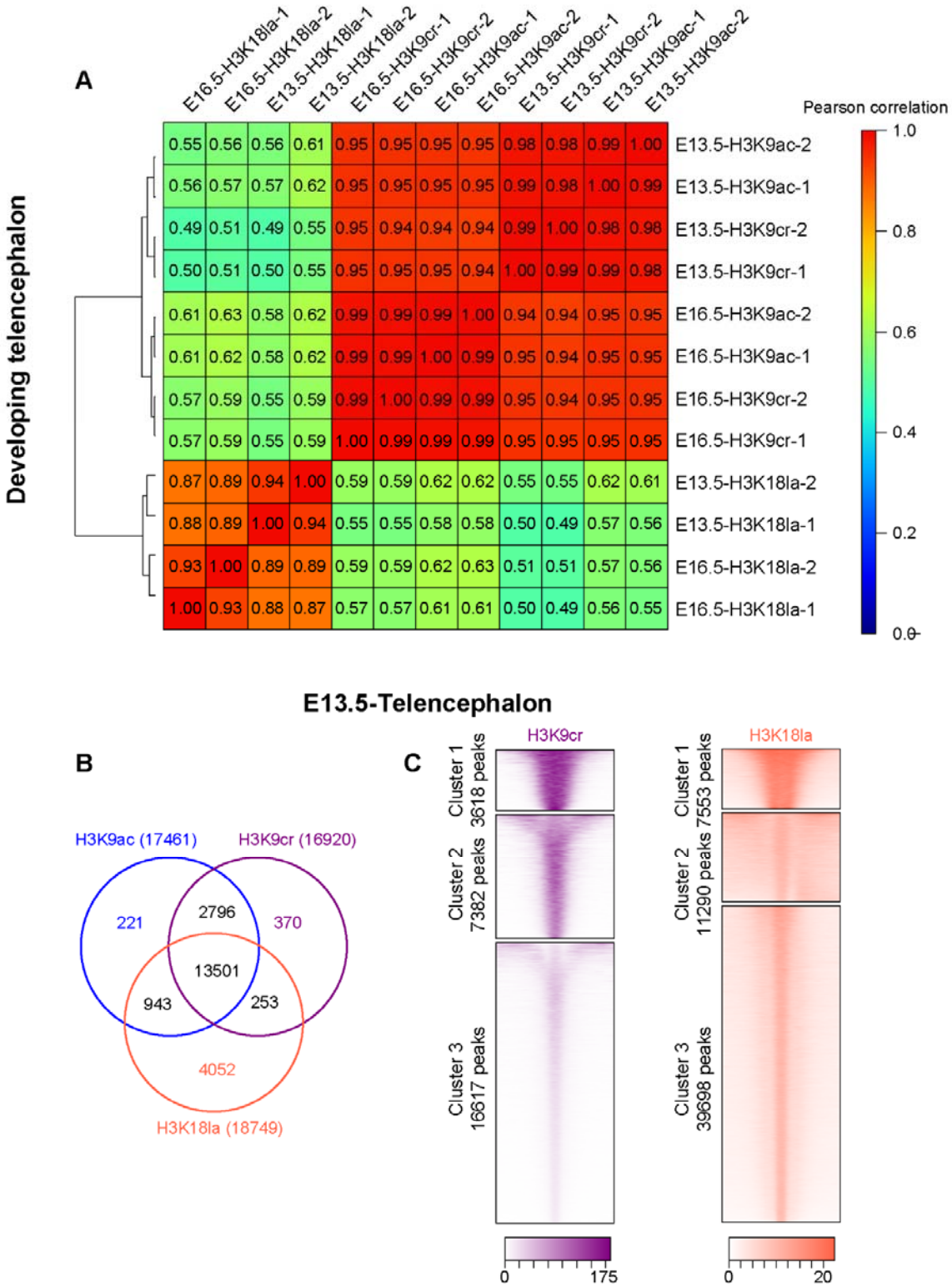

S3 Fig. Pearson correlation and cluster analysis of ChIP-seq data. (**A**) The pearson correlation of ChIP-seq data across different developmental stages. (**B**) Venn diagram of combined comparison of genes under regulation of H3K9ac (17461 genes), H3K9cr (16920 genes) and H3K18la (18749 genes) in the E13.5 telencephalon. (**C**) Heatmaps at peaks of H3K9cr and H3K18la (scaled by RPKM)

plotted within +/- 2.5 kb of the peak center (5’ to 3’) in the E13.5 telencephalon, which were divided to into three clusters and ranked from the highest to the lowest by ChIP signal, the number of peaks in each cluster was labelled on the left. Related to Fig 2.

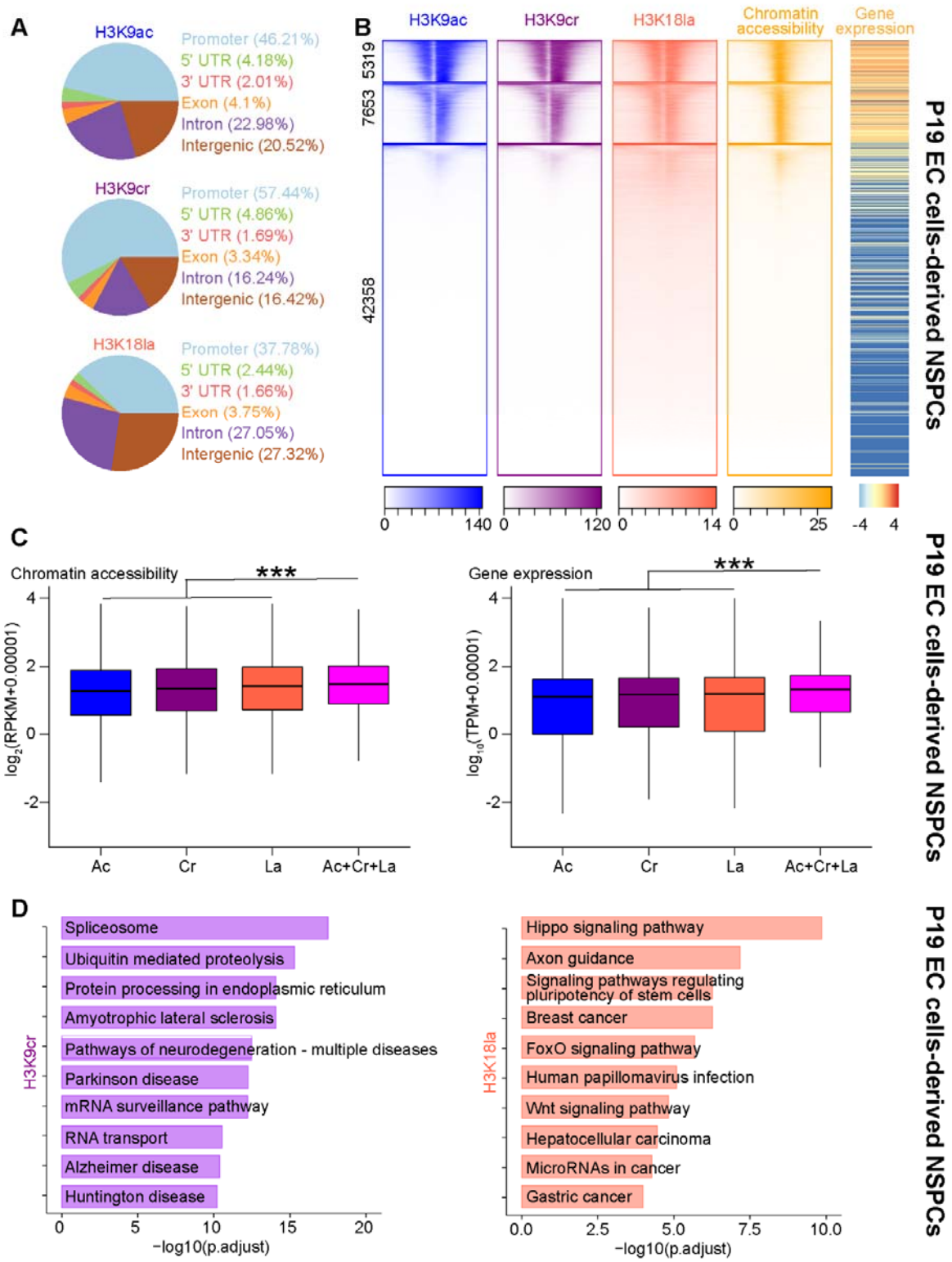

S4 Fig. Multi-omics profiling and functional annotation of H3K9cr and H3K18la in NSPCs. (**A**) Pie chart showing distribution of peaks of indicated histone marks at annotated genomic regions in the P19 EC cells-derived day 4 NSPCs. (**B**) Heatmaps of indicated histone marks intensity (scaled by RPKM), chromatin accessibility levels (scaled by RPKM) plotted within +/- 2.5 kb of the TSS (5' to

3'), and gene expression levels (scaled by $\log_{10}$(TPM+0.00001)) which were divided to into three clusters and ranked from the highest to the lowest by H3K9ac signal in the P19 EC cells-derived day 4 NSPCs, the number of genes in each cluster was labelled on the left. (**C**) Boxplot showing comparison of chromatin accessibility (left panel) and gene expression (right panel) across different groups of genes in the P19 EC cells-derived day 4 NSPCs. Ac, Cr, La and Ac+Cr+La: genes under regulation of H3K9ac (14450 genes), H3K9cr (13787 genes), H3K18la (12509 genes) and all three marks (10279 genes) respectively. (**D**) KEGG pathway enrichment analysis of genes under regulation of H3K9cr (left panel, 3960 genes) and H3K18la (right panel, 5638 genes) in the P19 EC cells-derived day 4 NSPCs. ***$P < 0.001$ by two-tailed unpaired Student's t-test in (C). Related to Fig 2.

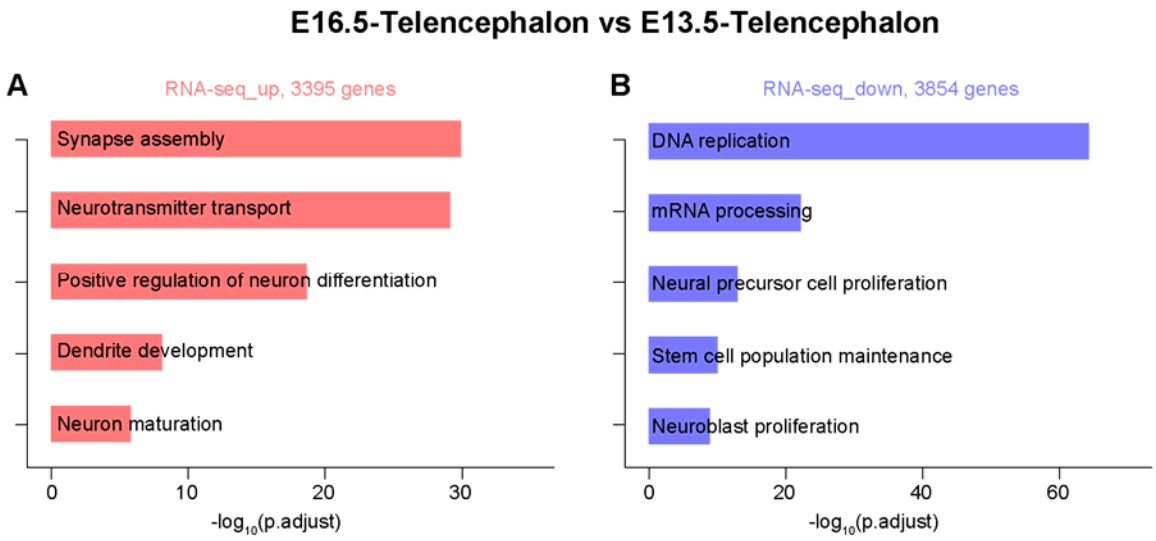

S5 Fig. Enrichment analysis of different expressed genes across developmental stages. (**A and B**) GO enrichment analysis (biological process) of up-regulated genes (A) and down-regulated genes (B) during neural development, which suggested cell fate transition across different stages of neurogenesis. Related to Fig 3.

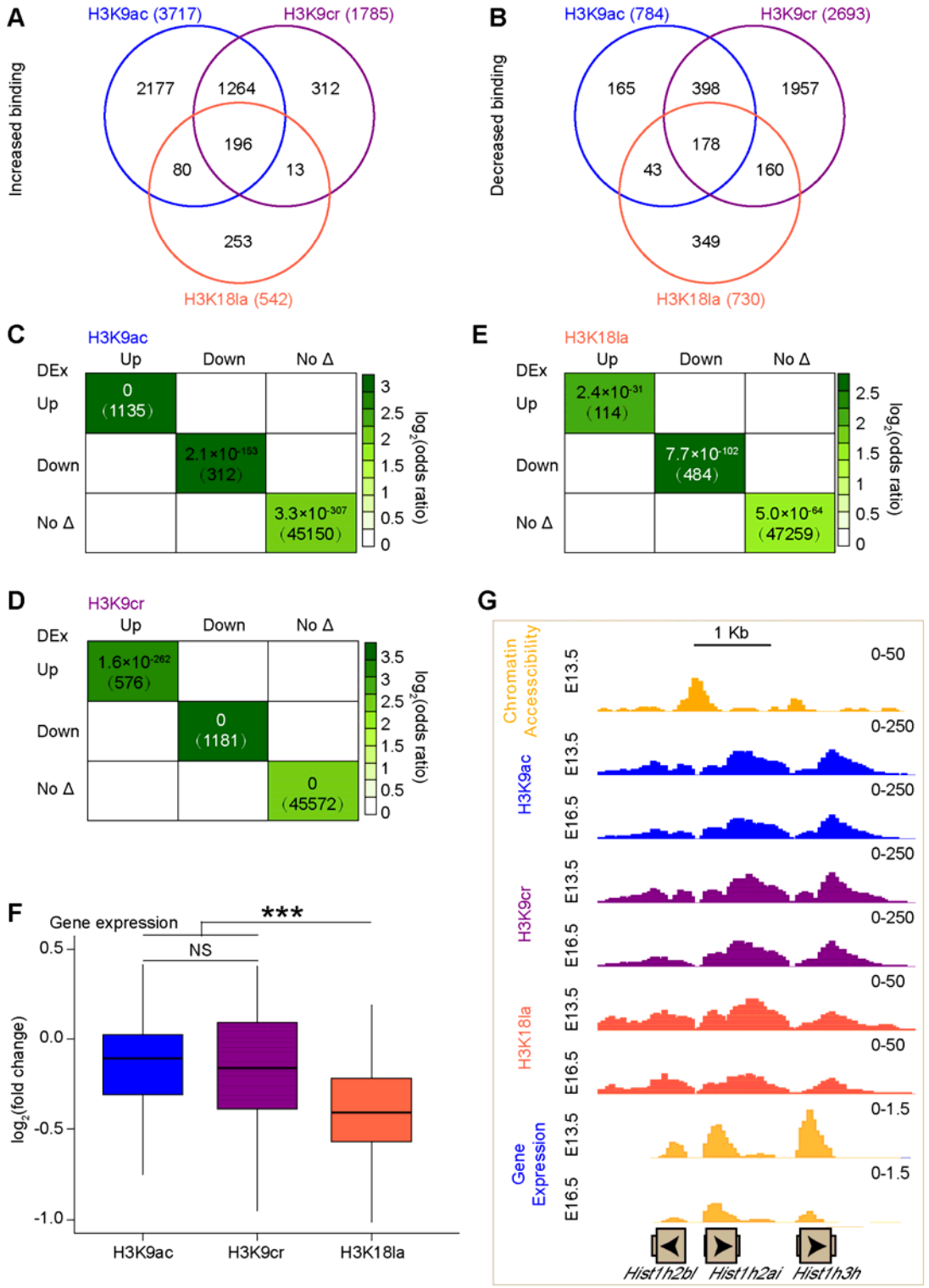

S6 Fig. Different binding analysis of histone lysine acylations in the promoter regions. (**A and B**) Venn diagram of a combined comparison of groups of genes with increased (A) and decreased (B) binding of each histone marks in the promoter regions respectively. (**C-E**) Odds-ratio analysis of overlapping genes displaying differential H3K9ac (C), H3K9cr (D) and H3K18la (E) enrichment

versus differential gene expression (DEx) respectively, insert numbers indicate respective P-values for associations, with the number of genes overlapping in parentheses. (**F**) Boxplot showing comparison of changes of H3K9ac, H3K9cr and H3K18la enrichment in the promoter regions of 70 genes encoding histones. (**G**) Representative genome-browser view at Hist1h2bl, Hist1h2ai, Hist1h3h gene of different sequencing data sets. NS, no significance; ***P< 0.001 by two-tailed unpaired Student's t-test in (F). Related to Fig 3.

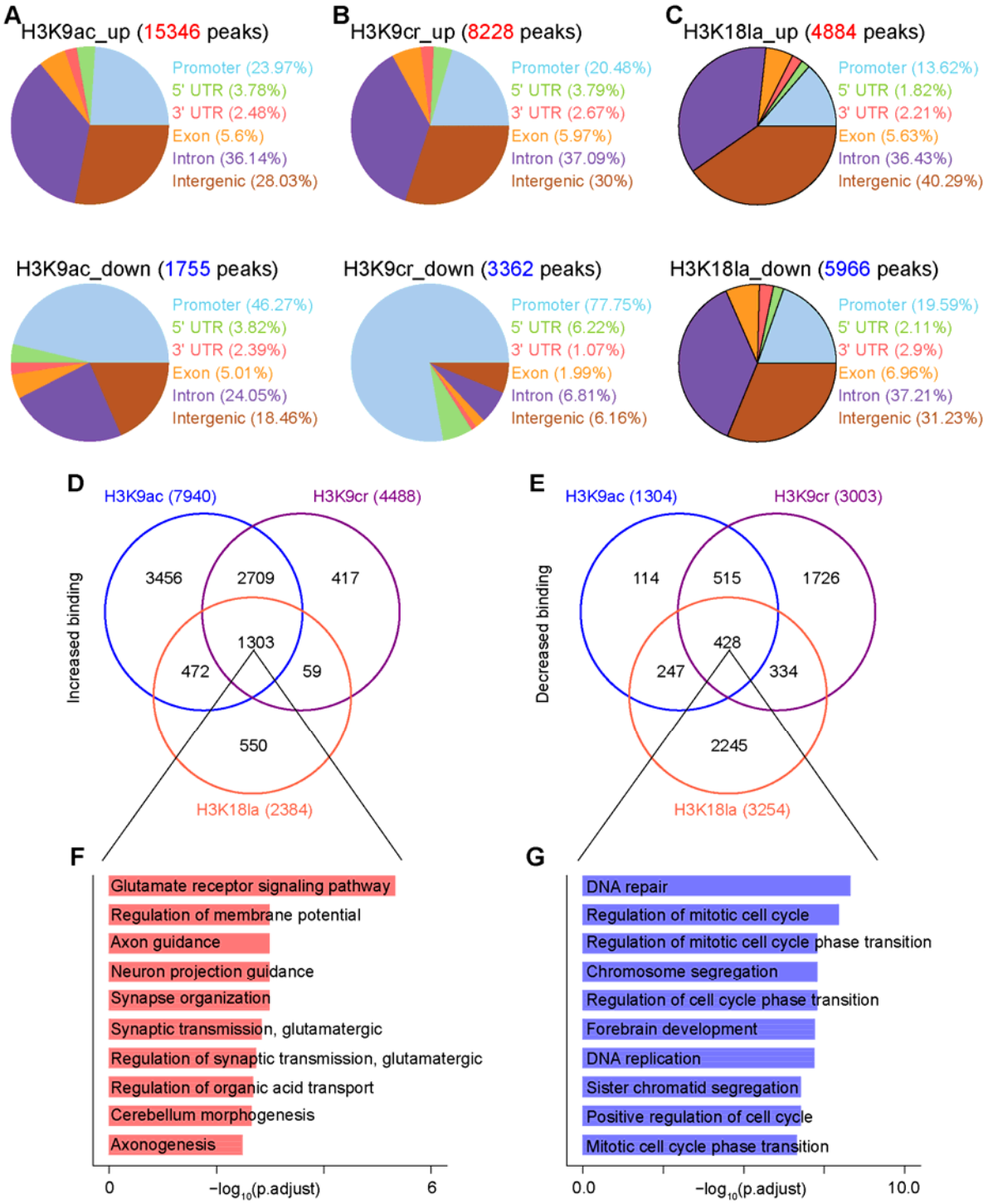

S7 Fig. Different binding analysis of histone lysine acylations in the peak regions. (**A-C**) Pie chart showing distribution of peaks with increased binding of H3K9ac (A), H3K9cr (B) and H3K18la (C) (top panels), and decreased binding of H3K9ac, H3K9cr and H3K18la (bottom panels) at annotated genomic regions respectively. (**D and E**) Venn diagram of a combined comparison of groups of genes under regulation of H3K9ac, H3K9cr and H3K18la, with increased (D) and decreased (E) binding of

each marks respectively. (**F and G**) GO enrichment analysis (biological process) of genes overlapped by increased (F) H3K9ac, H3K9cr and H3K18la binding (1303 genes), and decreased (G) H3K9ac, H3K9cr and H3K18la binding (428 genes), which suggested that these marks cooperatively regulated cell fate transition during neural development. Related to Fig 3.

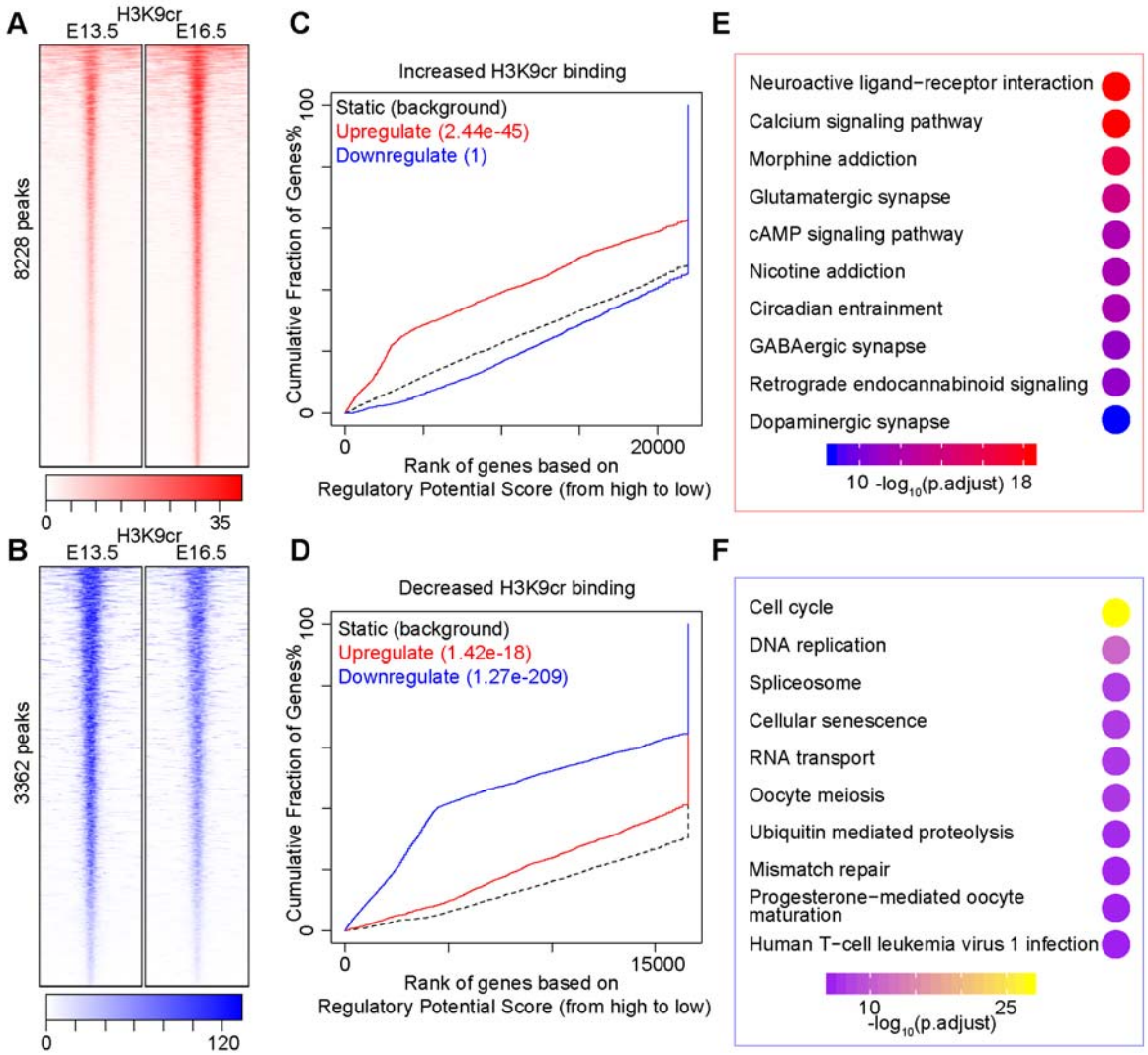

S8 Fig. Genome-wide dynamic changes of H3K9cr during neural development. (**A and B**) Heatmaps at peaks with increased (A) and decreased (B) H3K9cr binding (scaled by RPKM) plotted within +/- 5 kb of the peak center (5' to 3'), the number of peaks was labelled on the left. (**C and D**) BETA plot of combined computational analysis of H3K9cr ChIP-seq and RNA-seq data using peaks with increased (C) and decreased (D) H3K9cr binding respectively. (**E and F**) KEGG pathway enrichment analysis of up-regulated genes with increased H3K9cr binding (E) and down-regulated genes with decreased H3K9cr binding (F), there were 923 and 1342 genes in (E) and (F) respectively. Related to Fig 3.

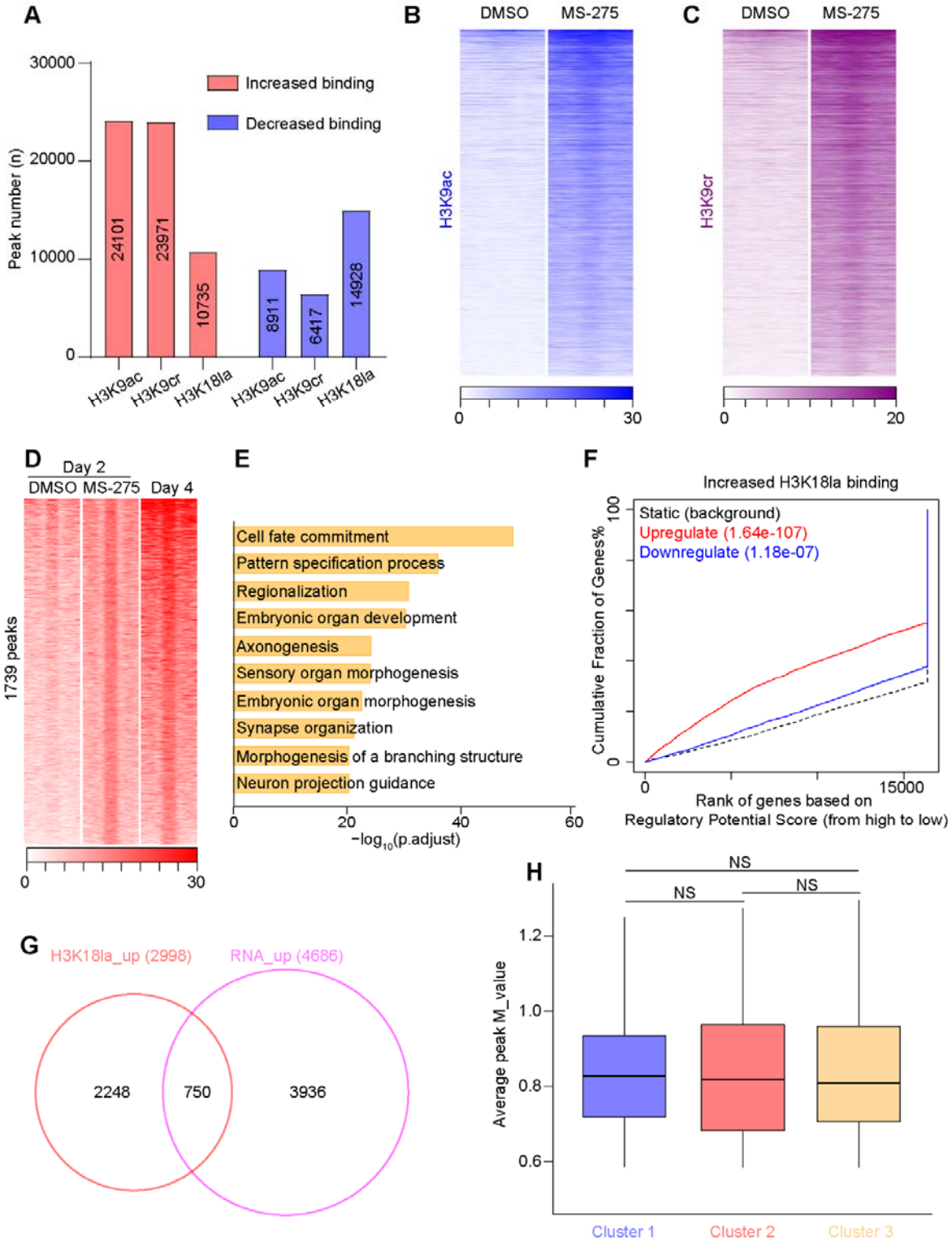

S9 Fig. Genome-wide alterations of indicated histone marks in differentiating NSPCs. (**A**) The number of peaks with different binding of indicated histone marks. (**B and C**) Heatmaps of H3K9ac (B) and H3K9cr (C) at peaks with increased H3K18la binding (scaled by RPKM) plotted within +/- 1 kb of the peak center (5' to 3') respectively. (**D**) Heatmaps of H3K18la ChIP-seq data of group of day

2 (DMSO), day 2 (MS-275) and day 4 NSPCs at peaks with increased H3K18la binding both in group of day 2 (MS-275) and day 4 NSPCs versus group of day 2 (DMSO) (scaled by RPKM) plotted with +/- 1kb of the peak center (5' to 3'). (**E**) GO enrichment analysis (biological process) of genes under regulation of these peaks in (D). (**F**) BETA plot of combined computational analysis of H3K18la ChIP-seq and RNA-seq data using peaks with increased H3K18la binding. (**G**) Venn diagram of a combined comparison of groups of genes with increased H3K18la binding and up-regulated expression after MS-275 treatment. (**H**) Boxplot showing comparison of changes of H3K18la levels across different groups of genes defined in Fig 6D. NS, no significance by two-tailed unpaired Student's t-test in (H). Related to Fig 6.

S1 Table. Summary of antibodies used in this study.

Antibody	Purpose	Company	Cat.Number	Dilution
anti-β-actin	Immunoblot	EASYBIO, Beijing, China	BE0033	1:2000-1:5000
anti-H3	Immunoblot	EASYBIO	BE7004	1:2000-1:5000
anti-HDAC1	Immunoblot	Sangon Biotech, Shanghai, China	D260479	1:1000
anti-HDAC2	Immunoblot	Sangon Biotech	D155199	1:1000
anti-HDAC3	Immunoblot	Sangon Biotech	D260481	1:1000
anti-H3K9ac	ChIP-seq	PTM Biolabs, Hangzhou, China	PTM-156	1.25 μg/ChIP-seq
	Immunoblot			1:1000
anti-H3K9cr	ChIP-seq	PTM Biolabs	PTM-516	1.25 μg/ChIP-seq
	Immunoblot			1:1000
	Immunostaining			1:1000
anti-H3K18cr	Immunoblot	PTM Biolabs	PTM-517	1:2000
	Immunostaining			1:2000
anti-H3K14la	Immunoblot	PTM Biolabs	PTM-1414	1:2000
	Immunostaining			1:2000
anti-H3K18la	ChIP-seq	PTM Biolabs	PTM-1406	3 μg/ChIP-seq

	Immunoblot			1:2000
	Immunostaining			1:2000
anti-H3K27ac	Immunoblot	Abcam	ab4729	1:2000
anti-Nestin	Immunostaining	Aves Labs	NES	1:500
anti-Pan-Kcr	Immunoblot	PTM Biolabs	PTM-501	1:1000
anti-Pan-Kla	Immunoblot	PTM Biolabs	PTM-1401	1:1000
anti-PAX6	Immunoblot	Invitrogen	14-9914	1:1000
anti-PCNA	Immunoblot	Cell Signaling Technology	13110	1:1000
anti RNA pol II	Immunoblot	Active Motif	39497	1:2000
anti RNA pol II CTD repeat phospho S2	Immunoblot	Abcam	ab193468	1:2000
anti RNA pol II CTD repeat phospho S5	Immunoblot	Abcam	ab193467	1:2000
anti-β-tubulin	Immunoblot	EASYBIO	BE3312	1:2000-1:5000
anti-TUJ1	Immunoblot	BioLegend	801202	1:1000
	Immunostaining			1:1000
donkey anti-rabbit Alexa Fluor 568	Immunostaining	Thermo Fisher Scientific	A10042	1:500
goat anti-chicken Alexa Fluor 594	Immunostaining	Thermo Fisher Scientific	A11042	1:500
goat anti-mouse Alexa Fluor 594	Immunostaining	Thermo Fisher Scientific	A11032	1:500

goat anti-rabbit Alexa Fluor 488	Immunostaining	Thermo Fisher Scientific	A11034	1:500
goat anti-mouse HRP	Immunoblot	EASYBIO	BE0102	1:2000-1:5000
goat anti-rabbit HRP	Immunoblot	EASYBIO	BE0101	1:2000-1:5000

S2 Table. Summary of ChIP-seq, ATAC-seq and RNA-seq data.

ChIP-seq

Sample name	Replicate	Total read pairs	Uniquely alignment rate (%)	Overall alignment rate (%)	Total peaks	Regulated genes
E13.5-Telencephalon-H3K9ac	1	53724013	65.26	98.54	37319	18574
E13.5-Telencephalon-H3K9ac	2	51131802	59.39	98.25	34532	18128
E13.5-Telencephalon-H3K9cr	1	46817521	61.41	97.89	32567	18115
E13.5-Telencephalon-H3K9cr	2	36679840	55.41	95.42	28968	17266
E13.5-Telencephalon-H3K18la	1	46396342	77.85	98.93	73369	20519
E13.5-Telencephalon-H3K18la	2	39864161	76.50	98.95	69157	20532
E16.5-Telencephalon-H3K9ac	1	45849859	67.10	98.77	49652	20996
E16.5-Telencephalon-H3K9ac	2	55471433	65.94	98.57	50668	21138
E16.5-Telencephalon-H3K9cr	1	44637264	69.87	97.33	41074	19925
E16.5-Telencephalon-H3K9cr	2	46975520	73.09	98.62	42304	20141
E16.5-Telencephalon-H3K18la	1	45649297	72.71	98.61	62073	18771
E16.5-Telencephalon-H3K18la	2	45469142	81.91	98.69	76037	20889
E13.5-Telencephalon-input	1	52415013	61.65	98.84	NA	
E13.5-Telencephalon-input	2	50313387	61.33	98.83		

E16.5-Telencephalon-input	1	41469169	60.83	98.83		
E16.5-Telencephalon-input	2	42552642	61.38	98.83		
P19-D4-NSPCs-H3K9ac	1	44385449	77.62	98.81	38703	19084
P19-D4-NSPCs-H3K9ac	2	46237774	78.24	98.72	37578	18881
P19-D4-NSPCs-H3K9cr	1	43443207	71.42	97.71	29280	17196
P19-D4-NSPCs-H3K9cr	2	43683550	70.49	98.06	28707	17184
P19-D4-NSPCs-H3K18la	1	43944019	67.43	98.43	54865	18212
P19-D4-NSPCs-H3K18la	2	54241452	70.70	98.46	51057	17951
P19-D4-NSPCs-input	1	47291008	66.42	98.56	NA	
P19-D4-NSPCs-input	2	46914207	64.76	98.57		
DMSO_P19-Day 2-H3K9ac	1	46696262	67.41	97.65	26555	16495
DMSO_P19-Day 2-H3K9cr	1	47324833	70.31	97.37	24874	16069
DMSO_P19-Day 2-H3K18la	1	41266344	65.67	98.57	36382	16778
MS-275_P19-Day 2-H3K9ac	1	39077351	72.25	98.46	84418	23736
MS-275_P19-Day 2-H3K9cr	1	61457579	62.95	97.91	70748	22251
MS-275_P19-Day 2-H3K18la	1	39838816	70.04	98.54	31577	9831
DMSO_P19-Day 2-input	1	53034910	56.35	98.46	NA	

MS-275_P19-Day 2-input	1	47774132	55.9	98.04	

ATAC-seq

Sample name	Replicate	Total read pairs	Uniquely aligned reads (%)	Total aligned reads (%)	Total peaks
E13.5-Telencephalon	1	32490761	31.78	61.84	26423
E13.5-Telencephalon	2	37379579	30.10	57.64	28207
P19-D4-NSPCs	1	42851384	39.35	95.77	28399
P19-D4-NSPCs	2	37858578	40.21	96.66	24420

RNA-seq

Sample name	Replicate	Total read pairs	Mapping rate (%)
E13.5-Telencephalon	1	20944513	81.45
E13.5-Telencephalon	2	22718954	81.37
E16.5-Telencephalon	1	22498548	77.93
E16.5-Telencephalon	2	23373976	77.11
P19-D0-ECCs	1	23547414	82.95
P19-D0-ECCs	2	22022756	82.73
P19-D4-NSPCs	1	23954541	81.42
P19-D4-NSPCs	2	22657641	81.78

P19-D8-Neurons	1	23707915	81.89
P19-D8-Neurons	2	22849732	81.32
DMSO_P19-Day 2	1	23809406	82.26
DMSO_P19-Day 2	2	22205497	81.58
MS-275_P19-Day 2	1	23019633	81.91
MS-275_P19-Day 2	2	23174365	81.14